



HAL
open science

In-situ coupled mechanical/electrical investigations on conductive TPU/CB composites: Impact of thermo-mechanically induced structural reorganizations of soft and hard TPU domains on the coupled electro-mechanical properties

Bienvenu Atawa, Léa Maneval, Pierre Alcouffe, Guillaume Sudre, Laurent David, Nathalie Sintès-Zydowicz, Emmanuel Beyou, Anatoli Serghei

► To cite this version:

Bienvenu Atawa, Léa Maneval, Pierre Alcouffe, Guillaume Sudre, Laurent David, et al.. In-situ coupled mechanical/electrical investigations on conductive TPU/CB composites: Impact of thermo-mechanically induced structural reorganizations of soft and hard TPU domains on the coupled electro-mechanical properties. *Polymer*, 2022, 256, pp.125147. 10.1016/j.polymer.2022.125147. hal-04289882

HAL Id: hal-04289882

<https://hal.science/hal-04289882>

Submitted on 16 Nov 2023

HAL is a multi-disciplinary open access archive for the deposit and dissemination of scientific research documents, whether they are published or not. The documents may come from teaching and research institutions in France or abroad, or from public or private research centers.

L'archive ouverte pluridisciplinaire **HAL**, est destinée au dépôt et à la diffusion de documents scientifiques de niveau recherche, publiés ou non, émanant des établissements d'enseignement et de recherche français ou étrangers, des laboratoires publics ou privés.

In-situ coupled electro-mechanical properties of conductive TPU/CB composites adjusted by thermo-mechanically induced structural reorganizations of soft and hard TPU domains

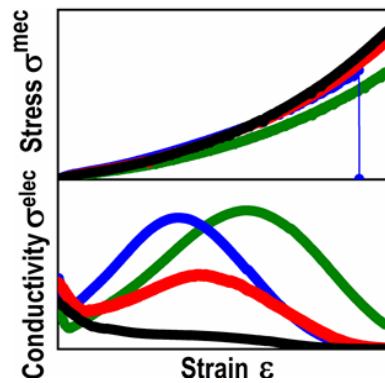
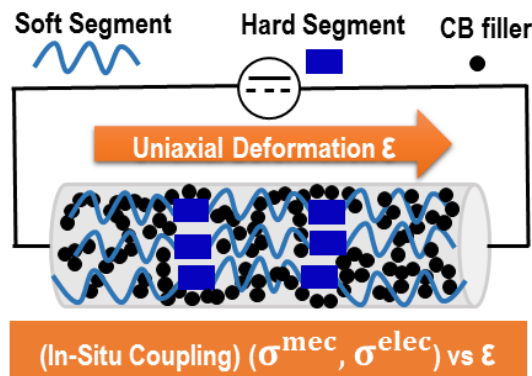
In-situ coupled electro-mechanical properties of conductive TPU/CB composites in relation to thermo-mechanically induced structural reorganizations of soft and hard TPU domains

Bienvenu Atawa, Léa Maneval, Pierre Alcouffe, Guillaume Sudre, Laurent David,

Nathalie Sintès-Zydowicz, Emmanuel Beyou, Anatoli Serghei

Université Claude Bernard Lyon, UCBL, CNRS, IMP UMR 5223, F-69622, Villeurbanne Cedex, France

Table of Contents Graphic



(for Table of Contents use only)

Abstract:

In-situ coupled mechanical/electrical investigations on TPU-based composite materials filled with carbon black have been carried-out under continuous and cyclic mechanical loading, with simultaneous measurements of stress, strain and electrical conductivity in dependence on the strain rate and amplitude. The impact of mechanical deformation and thermal treatment on the structure/properties relationship has been investigated by employing SAXS/WAXS, DSC and TEM measurements. Higher conduction properties were obtained by a strain induced crystallization of TPU soft domains that impacted the local concentration of CB aggregates above the percolation threshold. The TPU hard domains were found to be more sensitive to thermal treatment: annealing at high temperature led to microcrystalline hard domains that strongly influenced the conductivity evolution upon mechanical deformation. Structural and morphological reorganizations induced by mechanical deformation and thermal treatment can be thus efficiently used to adjust the coupled electro-mechanical behavior of TPU-based composite materials.

Corresponding author: anatoli.serghei@univ-lyon1.fr

1. Introduction

Thermoplastic polyurethanes (TPU) are versatile polymer materials used in our daily life for sporting goods, footwear and medical devices and in several technological fields, such as automotive, construction and electronics applications ¹. TPU possess the suitable mechanical properties of rubbers in terms of elongation, tensile strength ², and excellent abrasion and heat resistance ³, fatigue ⁴, resistance to solvents, oils and several other chemicals ². TPU are segmented multiblock copolymers composed of hard (HS) and soft segments (SS). HS and SS are poorly miscible, leading to the formation of a two-phase microstructure by microphase separation ⁴⁻⁸. The HS are formed of microcrystalline domains composed of polar compounds derived from diisocyanate and chain extenders that can easily aggregate into ordered hard domains (HD), while SS are usually separated into amorphous soft domains (SD) formed by polyol segments linking two HS ^{5,9-11}. Depending on the chemical structure and the ratio of SS and HS, TPU matrices are highly sensitive to the thermal ¹¹ and mechanical history ^{5,6,12}, strongly impacting the morphology and properties of TPU. Some microstructural evolution in TPU matrices can be evidenced through their thermal signature: the glass transition of either the SS or the HS, the endotherms associated to the ordering of disordered HS and those related to the loss of long range order of crystalline SD or HD ⁵. Generally, annealing induces strong morphological changes in TPU depending on the annealing temperature (below or above the T_g of SS or HS) ^{5,9,13,14}. From a model polyester-based TPU, Yanagihara and co-authors ⁶ reported an increase of the size and volume fraction of crystalline HD with annealing temperature. Surprisingly, they observed a decrease of the elastic modulus from 284 MPa at 25 °C down to 146 MPa at 145 °C possibly related to the evolution of the mechanical properties of the embedding soft matrix. Conductive fillers are usually added within TPU matrix in order to enhance conductivity properties ¹⁵⁻¹⁸. The resulting conductive composites are usually used as resistive sensors sensitive to their state of deformation ^{17,19,20}. In regards of the design of specific functional properties, numerous conductive carbonaceous fillers can be added within the insulating TPU matrix, paving

the way for wide applications in smart textile for human activity and health monitoring ²¹, speech recognition and intelligent robotics ¹⁹. Many authors considered the architecture of the conductive network as one of the key parameters to fully understand the electrical properties of these conductive composites when submitted to mechanical strain ²¹⁻²⁴. Lin and co-authors ¹⁵ designed several multi-wall carbon nanotubes (MWCNT) TPU-based strain sensors with tunable resistivity-strain sensitivity by modifying the architecture of the fillers. CB fillers were also added to the initial composite and two-filler MWCNT-CB composites were obtained. Furthermore, additional carboxylic acid functionalized MWCNTs (MWCNT-COOH) were used to enhance the interfacial interactions between the fillers and the matrix. When comparing the MWCNT composite with the MWCNT-CB composite, the conductive network obtained from the two fillers presented higher strain-sensitivity, whereas the MWCNT-CB conductive network could easily be destroyed under strain. Additionally, the highest sensitivity was obtained when combining the two fillers (MWCNT-CB) and MWCNT-COOH due to the concomitant effect of good stress transfer between the fillers and TPU matrix. Thus, smart properties of such conductive polymers are related to the fate of the conductive network under strain. The architecture of the conductive fillers and their evolution under strain, strongly impact the electromechanical properties of these conductive composites due to the modification of the number of conductive pathways and the tunneling distance between conductive fillers. The microstructural evolution of the polymer matrix induced by mechanical stress plays also an important role, impacting both mechanical and conductivity properties of the conductive composite. Wang and co-authors¹⁹, for instance, designed two CB/TPU films with adjustable scaffold fibrous microstructures presenting distinct resistivity-strain sensitivities, tensile strengths and elongations at break.

The ability of adjusting the composite structure and morphology represents thus a key factor for tuning the electromechanical behavior of composite materials, the latter being of great importance in many applications where monitoring in real-time the evolution of physical properties is required. This can be used for instance to evaluate the impact of transient or permanent changes occurring due to mechanical strain, fatigue, extreme deformations and structural or functional damages. An efficient approach to this purpose is employing in-situ coupled electrical measurements, the essential prerequisite being the optimization of the coupled

electromechanical behavior of composite materials. Tuning the electromechanical behavior is often realized during composite processing and relies in most of the cases on optimizing the polymer morphology and the properties of fillers used for the composite preparation. Much less explored in the scientific literature so far is the possibility of tuning the electromechanical behavior of composite materials *a posteriori* (after the composite processing), by external stimuli such as mechanical deformation or thermal treatment. In the present study, in-situ coupled mechanical/electrical investigations on TPU/CB composites are employed to show that large structural and morphological reorganizations of the soft and hard TPU domains can be obtained by mechanical deformation and thermal treatment and be efficiently used to adjust the coupled electro-mechanical behavior. Several studies have reported the resistivity-strain sensitivity of CB/TPU composites as discussed above^{17,19,25,26}, but none of them has thoroughly investigated the thermo-mechanically induced structural evolution of both SD and HD and its impact on the CB aggregates networks and the electrical properties. In the present article, we therefore proposed to systematically investigate the intricate relationship between structural and morphological reorganization of CB/TPU composites and their coupled electro-mechanical properties.

2. Materials and Methods

Materials: Commercially available carbon black filled TPU filament was purchased from Palmiga Innovation ltd. (ref. PI-ETPU 95-250 Carbon Black, Jonstorp, Sweden), with the following specifications: Diameter = 1.75 ± 0.05 mm, Density = 1.3 g/cm³, Volume Resistivity < 800 Ω·cm, elongation at break = 250% and yield strength = 15 MPa. The CB mass percentage of 30 wt% was determined by TGA measurements and detailed in section S1 of the supplementary information part. In order to characterize the polymer matrix alone, the CB fillers were extracted from the composite. The procedure consisted in dissolving 1 g of the composite in 50 mL of DMSO and extracting the CB fillers from the suspension by filtering using Millex-LCR hydrophilic PTFE membrane (0.45 μm pore size and 25 mm diameter). The absence of CB in TPU was therefore checked by

TGA as displayed in section S1 of the Supplementary Information Part. The neat polymer is a polyester-based TPU synthesized from methylenediisocyanate (MDI) as HS and poly (butylene adipate) (PBA) as SS. The molar ratio of the SD is three times that of the HD, conferring the flexibility properties to the monofilament. The mean molar masses were determined by size exclusion chromatography in DMSO at $T=70^{\circ}\text{C}$, without salt addition and equal to $M_n=25\text{ kg/mol}$ and $M_w=43\text{ kg/mol}$ ($D=1.7$). A detailed characterization by TGA, FTIR and RMN analyses is given in the supplementary section.

Differential Scanning Calorimetry: The differential scanning calorimetry analyses were carried out with a DSC Q200 from TA Instruments at 10 K/min under nitrogen flow with a rate of 25 mL/min. When necessary, the 5 mg sample was cooled down to -70°C at 10 K/min (for T_g evaluation) or directly heated from 20°C to 250°C at 10 K/min.

Coupled electrical and mechanical tests: The uniaxial tensile tests were performed with a Shimadzu AgX-plus tensile machine equipped with a 10 kN load cell at different crosshead speeds ranging from 0.1 mm/min up to 120 mm/min. The electrical measurements were carried-out during constant strain and cyclic tests at several strain magnitudes. The measurements were repeated at least three times at room temperature.

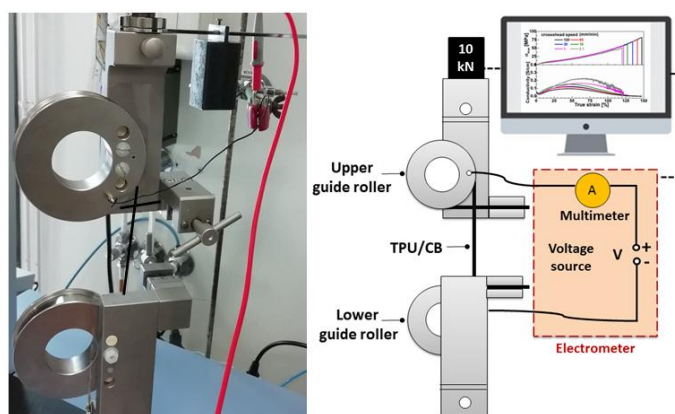


Figure 1: Experimental set-up for electromechanical measurement.

An initial sample length of 220 mm was used for all analyses and the true stress σ vs true axial strain ϵ mechanical behavior was calculated assuming isochoric deformation conditions. In order to record simultaneously the electrical and mechanical properties of the filament submitted to mechanical stress, homemade cord capstan tensile grips (appropriate for filament, rope, ribbon, wire) were designed to integrate the electrical measurement. The original TH 76 -20 rope grips were purchased from Rycobel Group Belgium. The grip was therefore modified in order to perform the electrical measurement. The two guide rollers were used as electrodes by isolating them electrically from the rest of the grips. The electrical connections were directly integrated on the guide roller and the electrical resistance of the CB/TPU composite was continuously recorded by a multimeter (Fluke 287).

Transmission electron Microscopy: The microscopy analyses were performed for a fresh non-stretched sample (as the reference state) and stretched samples (up to breakage) at strain rates of 120, 10 and 0.1 mm/min. The samples were prepared by cryo-ultramicrotomy (Leica UC7) at -100°C and slices of 80nm were placed on copper grids for observation. The images were recorded on a Transmission Electron Microscope JEOL 1400 Flash using an acceleration voltage of 120 KV. The images were analyzed with Image J software in order to gain quantitative information on the overall area occupied by aggregated or isolated CB fillers, their individual areas and the domains free of CB. We used the trainable segmentation plugin in order to differentiate the domains filled and free of CB. This plugin combined a collection of machine learning algorithms trained to learn from the user input and perform later the same task in the overall data ²⁷. The overall area was subdivided into two domains: the first domain is made of isolated or aggregated CB fillers and the second domain was denuded of CB. The main parameters used to analyze the samples were the size of the aggregated CB filler and the pathways of CB free domains.

WAXS and SAXS: WAXS and SAXS measurements were performed concomitantly on the D2AM beamline of the European Synchrotron Radiation Facility (ESRF) in Grenoble. The sample was taped on a home-made cylindrical sample holder with a hole in the middle and submitted to an incident X-Ray beam. The photon energy was set to 15.7 keV and the cross section of the incident beam was $0.42 \times 0.45 \mu\text{m}^2$. The SAXS intensities were collected using the 2D D5 detector placed at a distance of 1.84 m from the sample. The WAXS intensities were collected using the IMXPAD WOS-S700 X-ray detector placed at a distance of 15 cm from the sample. The exposure time was set to 10 s. The scattering vector q -calibration ($q = 4\pi \sin(\theta) / \lambda$, where θ is half of the scattering angle, and $\lambda = 0.78968 \text{ \AA}$ is the incident beam wavelength) was realized with a silver behenate standard for SAXS and lanthanum hexaboride (LaB_6) standard for WAXS. The scattering diagram $I(q)$ vs q (\AA^{-1}) were corrected by subtracting the contribution of the sample holder from the scattering intensity of the sample.

3. Results and discussions

3.1 Calorimetric behavior of neat TPU and CB/TPU

The thermal fingerprint of neat TPU and CB/TPU was investigated by DSC in order to identify the different phase transformation processes occurring in both samples. The samples were previously heated from 30°C up to 250°C at 10K/min and cooled down to -70°C at 20K/min . The thermogram showed in figure 2 presents the heating scan of both samples at 10K/min from -70°C up to 250°C .

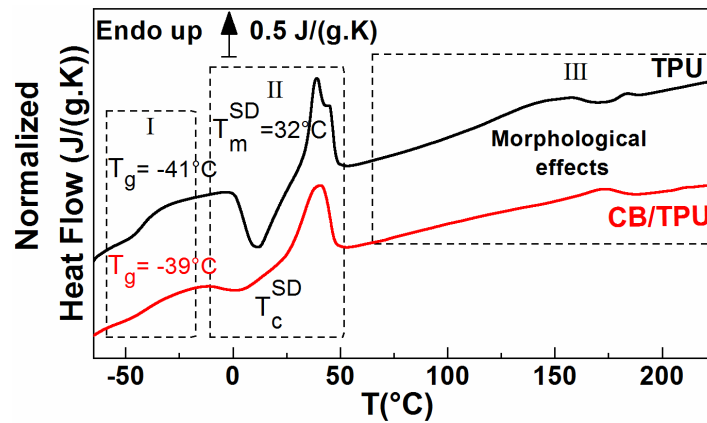


Figure 2: DSC thermograms of melt-quenched TPU and CB/TPU composite at 10 K/min.

Both samples illustrated the same thermal events and the thermograms can be subdivided into three temperature domains:

For neat TPU the first domain I represents the glass transition region with a T_g of the SD at $-41 \pm 1^\circ\text{C}$ and $\Delta C_p = 0.25 \text{ J/g}$. This value is consistent with literature data. Aurilia and coworkers¹³ reported a $T_g^{\text{SD}} = -55^\circ\text{C}$ for a polyether based TPU while Yanagihara and co-authors found a $T_g^{\text{SD}} = -14^\circ\text{C}$ for a polyester based TPU. The glass transition was slightly impacted by the presence of the filler. Dong and coauthors²⁵ reported that the T_g^{SD} drops from -27°C down to -30°C when increasing the content of CB fillers from 0 to 12 wt %. In the case of CB/TPU, the T_g^{SD} slightly increases by 2°C and the heat capacity jump at T_g strongly drops by almost 74% ($\Delta C_p = 0.07 \text{ J/g.K}$) compared to neat TPU. This behavior is due to the increase of the SD crystalline fraction in TPU matrix enhanced by the presence of CB particles. No evidence of the glass transition associated to the HD was mentioned for both samples, suggesting that the HD are mostly crystalline.

The second region II corresponds to the crystallization and melting of the SD in both neat TPU and CB/TPU. The SD crystallization onset temperature is 12°C higher for neat TPU compared to the composite. Additionally, the SD crystallization enthalpy in neat TPU ($\Delta H_c \sim 13 \text{ J/g}$) is more than 3 times higher than the SD crystallization enthalpy in the composite ($\Delta H_c \sim 4 \text{ J/g}$). Nevertheless, the SD melting temperature in both samples was identical ($T_m^{\text{SD}} = 32^\circ\text{C}$) with a melting enthalpy $\Delta H_m^{\text{SD}} = 13 \text{ J/g}$. This could suggest that the

quenched TPU polymer contains a higher amorphous fraction in comparison to the composite. Since the SD crystallization enthalpy equalized that of the melting enthalpy in neat TPU, the SD of the quenched sample can be considered as purely amorphous. The thermal events occurring in region III are related to the morphological changes occurring in HD and to order-to-disorder transitions through the loss of long and short-range order within hard domains^{9,13}.

3.2 Electromechanical properties

The coupled mechanical/electrical properties of CB/TPU composite were investigated at room temperature under different conditions as follows: a) under variable strain rates ranging from 0.1 mm/min to 120 mm/min b) during continuous iso-strain conditions for 10 min at each selected strain magnitude from 1% up to 240% at a loading rate of 10 mm/min c) under 20 loading/unloading cycles at selected maximal strains from 2.5% to 200%. The main objective is to understand how mechanical stretching can modify the electrical response of the conductive TPU/CB composite and the microscopic origin of this behavior. Figure 3a illustrates the stress-strain behavior and Figure 3b) displays the failure strength vs strain at failure of CB/TPU composite at cross head speeds varying between 0.1 and 120 mm/min. The corresponding true strain rates at zero strain and the strain rates at breakage are displayed in table 1.

Table 1: True deformation rates at zero deformation $\dot{\epsilon}_i$ and at breakage $\dot{\epsilon}_R$

v (mm/min)	0.1	1	10	30	60	120
$\dot{\epsilon}_i \text{ min}^{-1}$	4.5×10^{-4}	4.5×10^{-3}	4.5×10^{-2}	1.4×10^{-1}	2.7×10^{-1}	5.5×10^{-1}
$\dot{\epsilon}_R \text{ min}^{-1}$	3.8×10^{-6}	3.7×10^{-5}	3.7×10^{-4}	1×10^{-3}	2×10^{-3}	3.7×10^{-3}

As usually observed for filled elastomers, the stress-strain behavior is nonlinear and can be described into three stages displayed as follows: at low strain region ①, a gradually decrease tangent modulus followed by a nearly constant tangent modulus in region ② and increasing tangent modulus at high strain region ③.

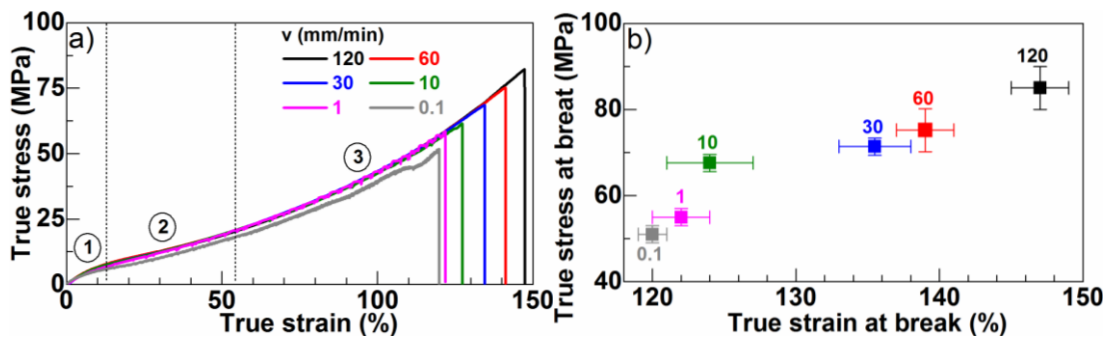


Figure 3: a) Stress-strain curve of CB/TPU composite at different loading rates from 0.1 up to 120 mm/min. b) Failure plot (stress at break vs strain at break) at different loading rates from 0.1 up to 120 mm/min.

The modulus drop off described at low strain region is usually attributed to loss of filler-filler and filler-matrix adhesion^{28,29}. In fact, the percolated CB filler network can entrap some polymer chains in such a way that the CB/TPU composite mechanically behaves as a unique CB filler network. Consequently, the elastic modulus of the composite cannot be directly measured at the origin of the stress-strain curve.

Assuming that the composite is isotropic in undeformed state, the volume changes associated with deformation are very small and may be neglected, the true stress under uniaxial stretching can be written as function of the elastic modulus E and given by:

$$\sigma_{true} = \frac{E}{3} \left(\lambda^2 - \frac{1}{\lambda} \right) \quad (1)$$

where the extension ratio $\lambda = 1 + \varepsilon_N$ with $\varepsilon_N = \frac{\Delta l}{l_0}$ the nominal strain. The following approximation can be made for small strain provided the third order terms in ε_N are neglected: $\left(\lambda^2 - \frac{1}{\lambda} \right) \equiv 3\varepsilon_N$ and Hooke equation can be derived:

$$\sigma_{true} = E\varepsilon_N \quad (2)$$

The modulus can be determined by plotting σ_{true} as function of $(\lambda^2 - 1/\lambda)$, as shown in figure 4. The modulus value measured at small strain $E_1 = (85 \pm 6 \text{ MPa})$ was associated to the backbone of the CB percolating network. When this CB network is broken, the calculated modulus value $E_2 = (21 \pm 3 \text{ MPa})$ can be linked to the TPU matrix. Both modulus are strain rate insensitive. This could suggest that these parameters are related to intrinsic properties of the fillers and the matrix.

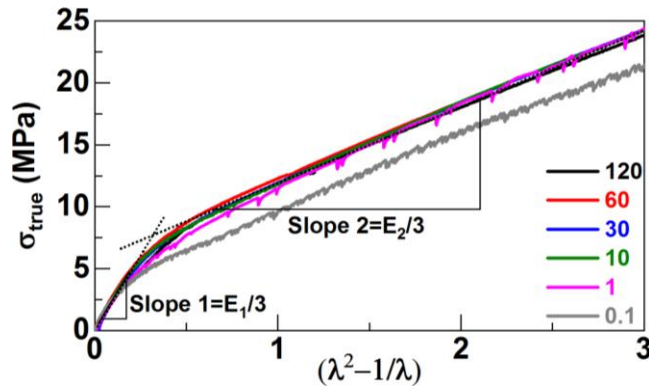


Figure 4: Evolution of the σ_{true} as function of $(\lambda^2 - 1/\lambda)$ for small strain.

Nevertheless, the CB/TPU composite is strongly rate-sensitive, with the magnitude of the stress and the strain at break increasing by 40% and 20% respectively over the loading rate range. The stress at break increased from 51 ± 2 MPa to 85 ± 5 MPa when increasing the crosshead speed from 0.1 mm/min to 120 mm/min. More interestingly, the strain at break also increased from $120\% \pm 1\%$ to $147\% \pm 2\%$ for the same crosshead speeds variation. The strain rate can highly impact the mechanical properties of filled or non-filled elastomers regarding the viscoelastic nature of the polymer³⁰. The increase of stress at failure ϵ_R with strain rate is usually due to the reduction of the molecular mobility of the polymer chains that becomes stiffer. Moreover, it is generally observed that the strain at failure decreases with increasing strain rate since the polymer chains do not have enough time to relax and dissipate the mechanical stress at high loading rates leading to bond rupture³¹⁻³⁴. Moghim and coworkers³¹ reported a strain rate sensitivity in mechanical properties of neat PU. This strain rate sensitivity diminished for MWCNT/PU nanocomposite. When the strain rate varied in the range $12 \times 10^{-4} \text{ min}^{-1}$ to $12 \times 10^{-1} \text{ min}^{-1}$, the stress at failure of neat PU increased by 60% while that of the composite (PU-1wt% CNT) increased by 15%. Moreover, the elongation at break for the nanocomposite is strain-rate insensitive while for neat PU, it diminishes by 50% when increasing the strain rate in the same range. The incorporation of MWCNT in PU may increase the loss of molecular mobility, increasing the tensile strength while diminishing the strain rate sensitivity. Hussein³⁰ reported an opposite behavior for CB reinforced butyl based elastomers. The strain at break ϵ_R increases for almost 19% when increasing the strain rate from 6×10^{-4} to $6 \times 10^{-1} \text{ min}^{-1}$. The loading rate sensitivity of the strain at break increases by more than 40% for a CB reinforced butyl rubber (60 wt%) blended with polyethylene (40 wt%). Nevertheless, the reinforcement effect due to CB filler diminished in the blended composite since the strain at failure occurred at lower strain values in comparison to the CB reinforced butyl rubber (100 wt%). The gain in strain rate sensitivity can be related to poor adhesion between filler-polymers and polymer-polymer. The strain rate sensitivity on mechanical properties at break described by Hussein³⁰ was reported in the present study for CB/TPU. Such behavior is far from being conventional and results from subtle structural evolution occurring in the composite itself. Boyce and Qi¹¹ reported that the stress-strain behavior of neat TPU is subjected to loading rate sensitivity that originates

from internal energy change due to deformation of the HD. It seems that the incorporation of CB in the TPU matrix does not prevent from frictional interactions amongst different HD neither from the breakage nor formation of hydrogen bonds implicated in the rearrangement of the hard domains. Therefore, the strain rate sensitivity of CB/TPU composite must be tackled as a consequence of stretching-induced morphological modifications of both HD and SD and their interactions with the filler. The strain rate sensitivity of the mechanical properties at break of CB/TPU is directly related to the structure of the polymer and its interactions with the CB particles. In the following paragraph, the architecture of these fillers through the evolution of the electrical properties of CB/TPU composite under different mechanical deformation is explored. The electrical response of the conductive CB/TPU composite was measured upon stretching at various crosshead speed ranging from 0.1 mm/min to 120mm/min. Depending on the strain applied; three distinct regimes could be defined independently of the loading rate as displayed in figure 5 a).

Regime I: At low strains ($\epsilon < 6\%$), the conductivity slightly decreases by 20% to 40% of its initial value, independently of the loading rate. For example, under stretching at 0.1 mm/min the conductivity slightly diminishes from 0.049 S/cm to 0.032 S/cm with the minimum conductivity at $\epsilon = 3\%$.

Regime II: the conductivity strongly increases for $\epsilon > 6\%$ and reaches a maximum value for a true strain ϵ between 47% and 69% depending on the loading rate. For example, at 0.1 mm/min loading rate, the conductivity increases from 0.031 S/cm to 0.223 S/cm with the maximum conductivity at $\epsilon = 69\%$.

Regime III: The last regime corresponds to a decrease of conductivity upon stretching at large strains and the final loss of conduction properties at break. For example, for a strain rate of 0.1 mm/min, the conductivity continuously decreases (for strain $> 69\%$) from 0.223 S/cm to 0.055 S/cm before failure occurs at $\epsilon = 120\%$. When changing the strain rate, the three regimes still persists. Nevertheless, the conductivity values at their maxima were higher for low stretching rates (0.223 S/cm at 0.1 mm/min, 0.163 S/cm for 1 mm/min, 0.153 S/cm for 10 mm/min and 0.094 S/cm for 120 mm/min). Moreover, the maximum of conductivity vs “true strain” shifts with the crosshead speed. This suggests a kinetic process related to the stretching rate and governing the strain position of the maximum conductivity and its magnitude.

Low stretching rates promoted the formation of a conducting CB network, related to the relaxation of the TPU macromolecular chains. On the contrary, high stretching rates do not promote full relaxation of the polymer chains and the CB fillers are not sufficiently connected to build the most conductive channels. This effect is consistent with other works related to the conduction properties of TPUs filled with platelet-like conducting fillers: Liu and coworkers analyzed the effect of loading rate on the strain sensing behavior of TPU/graphene composites. For a nominal strain amplitude of 30%, the relative resistance R/R_0 (R is the real time resistance and R_0 the initial resistance of the sample) at loading rates of 0.1 min^{-1} , 0.3 min^{-1} and 0.5 min^{-1} are about 450%, 550% and 650% respectively suggesting more destruction of graphene conduction pathways (or less contacts establishments) at higher loading rates ³⁵. However, the authors identified neither the increase of conductivity nor the three regimes mode upon stretching.

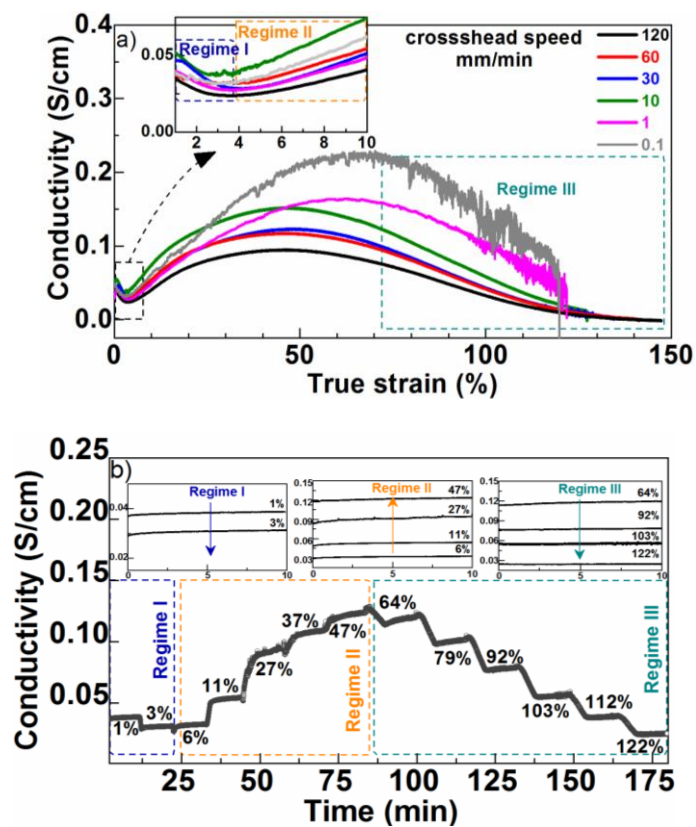


Figure 5: a) Evolution of the conductivity as function of strain for several crosshead speeds for CB/TPU samples b) Iso-strain evolution of the conductivity as function time for CB/TPU samples with a loading rate of 10 mm/min. The insert figures illustrate the relaxation behavior of conductivity in three distinct regimes.

In order to confirm the relation between chain relaxation and filler conduction micro pathways in CB/TPU, a continuous iso-stretching was performed. The conductive composite was stretched at 10 mm/min loading rate to various strains ranging from 1% to 122% and maintained for 10 min at each strain. Figure 5b illustrates the time evolution of the conductivity upon stretching for increasing strains. The three conduction regimes are clearly identified and seem related to intrinsic changes of CB/TPU electrical properties. As depicted in the insert figures, conductivity relaxes slightly towards higher values at constant strain in regime I, II and the beginning of regime III ($\epsilon=64\%$). At higher strain the conductivity remained unchanged at constant strain. The first observation may suggest a weak self-healing process of the broken CB interconnections at constant strain, while at $\epsilon>64\%$, the CB interconnections are irreversibly destroyed.

During stretching, two competing mechanisms taking place concomitantly can be considered: the creation of new conduction channels with aggregates and CB particles getting closer in the transverse direction, and the breakage of existing contacts in the axial direction³⁶. Three different regimes can be defined, as follows:

Regime I: The decrease in conductivity occurring in the first regime suggests a moderate disconnection between neighboring conducting CB particles during the early stages of deformation. *De facto*, the conductivity evolution is controlled by an initial separation of the conducting fillers in the TPU matrix at small strains.

Regime II: The increase in conductivity during the second regime for higher strains ($6\%<\epsilon\leq 47\%$) suggests that the viscoelastic/plastic behavior of the TPU allows filler displacement and/or rotation in such a way that re-entanglement of neighboring CB particles globally result in the creation of new conduction channels, prevailing on the opposite phenomena.

Regime III: At extreme strains, a progressive loss of percolation occurs. In the axial direction, the distance between neighboring CB conducting fillers increases as the elongation magnitude increases until damage and

rupture. High strains promote severe disruption to the conductive network and lead to larger gaps between conductive fillers and filler aggregates, causing the decrease of conductivity³⁵. The decrease of conductivity under mechanical loading is reported for several conductive TPU composites^{15,16,21,37,38}. Lin et al. reported the decrease of electrical conductivity under stretching at 5 mm/min (0% to 275% nominal strain magnitude) from 6.7 S/cm to 3.85 S/cm for PU composite containing 10 wt % MWCNTs. The decrease of conductivity was even higher for a PU composite containing 2 wt % MWCNT, 7 wt % CB and 1 wt% MWCNT-COOH: conductivity diminished from $6.7 \cdot 10^{-2}$ S/cm down to 10^{-5} S/cm under stretching at 5 mm/min [16].

Quite evidently, the nature of the filler highly govern the conduction behavior upon stretching. Graphene and CNT fillers are likely to be oriented in the stretching direction^{15,35} promoting axial percolation while in the transversal direction the percolated network may be destroyed. The competition between longitudinal percolation and transversal depercolation due to the anisotropy of graphene and CNT fillers may explain why in CNT/graphene filled polymers the increase of conductivity (regime II) is rarely observed. In the case of CB filled polymers, axial repercolation should prevail on transverse depercolation due to the anisotropy of the CB aggregates. Flandin et al. reported a four-regime mode in resistivity for CB-filled ethylene-octene elastomer²⁸. In their work, regime I appeared as a decrease in conductivity from 0.08 S/cm to 0.056 S/cm for $\epsilon_N \leq 3\%$ due to the initial breakage of CB conductive network. Regime II was expressed as an increase in conductivity from 0.056 S/cm to 0.17 S/cm for $3\% \leq \epsilon_N \leq 30\%$ possibly due to a reversible rearrangement within the weakly bonded secondary aggregates. Regime III was reported as the recoverable damage strain domain appeared as a decrease of conductivity down to (10^{-3} S/cm) for $\epsilon_N \leq 600\%$. Regime IV known as the depercolation regime appeared as a decrease of conductivity for $\epsilon_N \geq 600\%$. In the case of CB/TPU composite, regimes III and IV can be hardly deconvoluted and are considered as one single regime. Thus, the question of reversibility of the filler rearrangement, in particular during regime II is raised up. To address it, cyclic loading/unloading investigations were carried-out in the present study.

Impact of uniaxial loading/unloading cycling on in-situ coupled mechanical/electrical properties

In this section, the electrical properties of CB/TPU composite were measured during load/unload cycles at different strain amplitudes. The conductivity of the composite was monitored during 20 loading/unloading cycles at various maximal strains ϵ_{\max} ranging from 2.5% to 110% at 10 mm/min. Figure 6 a) b) and c) shows the cyclic strain evolution of stress and conductivity for an ϵ_{\max} of 2.5%, 56% and 110%, respectively. For clarity, the cyclic loading/unloading stress and conductivity behavior at ϵ_{\max} equal to 5%, 10%, 41%, 81% and 92% are presented in the supporting information. Figure 5d) resumes the stress and conductivity evolution for ϵ_{\max} equal to 2.5%, 5%, 10%, 41%, 56%, 81%, 92% and 110% over 20 loading/unloading cycles. The evolution of *stress versus strain* is irreversible along a loading/unloading cycle:

At $\epsilon_{\max} = 2.5\%$, *i.e.* in regime I, the residual strain between the first loading and the unloading curves is close to 0.5%. The residual strain becomes insignificant from the second cycle and the hysteresis is weak between the loading and unloading stress-strain curves. Additionally, stress softening is relatively low between the first and the 20th cycle (from 2.6 MPa to 2.3 MPa). Mechanical properties become stable after a few cycles (about 10 cycles). At such low ϵ_{\max} , the mechanical properties rapidly recovered since the stretching is performed mainly in the elastic regime of CB/TPU composite.

At medium values of ϵ_{\max} ($\epsilon_{\max} = 56\%$), 34% residual strain was evidenced between the first loading and unloading stages. At the second cycle the residual strain between loading and unloading diminishes to 3%. The residual strain between loading and unloading disappears from the 3rd cycle while strain hardening continued between the 2nd and 15th cycle for almost 11%. The stress-strain curve was stabilized from the 15th cycle. Between the first and the last cycle a stress softening occurred, with a decrease of the stress at ϵ_{\max} of 4 MPa.

At large ϵ_{\max} ($\epsilon_{\max} = 110\%$), strong dissipation occurs since the residual strain between the loading and unloading stages reaches a value of 83%. In the second cycle, the residual strain between loading and unloading decreases to 8%, while strain softening evaluated at ϵ_{\max} continued between the 2nd and 15th cycle to almost 21%. The stress-strain curve was stabilized from the 15th cycle and a total stress softening of 9 MPa

was reported between the first and last cycle. All these mechanical features are in accordance with the so-called Mullins effects observed in filled and non-filled elastomers³⁹⁻⁴². Such softening effect has already been reported for neat TPU¹¹, and MWCNT/TPU composites [51]. Mullins and Tobin⁴¹ explained the softening phenomenology as a result of the microstructure evolution due to a quasi-irreversible (i.e. reversible only after high temperature thermal treatment) rearrangement of both the molecular and the filler networks appearing during stretching. The loading/unloading cyclic conductivity-strain evolution at different strain maxima ϵ_{\max} can provide specific information regarding the microstructural changes and the conductivity channels built by the CB aggregates.

At low ϵ_{\max} (2.5%), the conductivity decreases upon loading from 0.035 S/cm down to 0.021 S/cm during the first loading (i.e. a behavior observed as regime 1 figure 4b). In contrast, upon unloading, there is a significant recovery of conductivity from 0.021 S/cm to 0.026 S/cm, showing that filler network structural change stays limited. The same behavior can be mentioned for strain maximum at 5% and 10% but this time the recovery of conductivity is more pronounced upon unloading and the conductivity value can overpass that of the unstressed sample (Fig. S4 from SI). From the 2nd loading/unloading cycle, the conductivity upon loading stays higher than the unloading conductivity with a maximum variation of 4%. Moreover, the electrical conductivity at $\epsilon_{\max} = 2.5\%$ increases with cycling until a maximum 0.270 S/cm and stabilizes after 15 cycles. Thus, even for small ϵ_{\max} , the 1st loading may induce small displacement of CB filler creating interfiller contacts and the unloading step may enhance the repair of disrupted conductivity channels during the loading stage. Thus, the two processes of filler rearrangements are at work to preserve and increase connectivity. From the 2nd cycle, loading/unloading significantly promotes the creation of suitable conductivity channels until an equilibrium cycle is reached both for mechanical and conductivity properties.

At medium values of ϵ_{\max} (56%), the conductivity increases from 0.035 S/cm to 1.12 S/cm upon first loading and decreases down to 0.066 S/cm during the unloading step. At the 2nd cycle, the conductivity upon loading is always higher than upon unloading (with a maximum difference of 10 %) in the strain range 34%-44%; for $\epsilon > 44\%$, the unloading conductivity overpasses the loading value (with a maximum difference of 9%). Loading

and unloading conductivities curves cross at $\epsilon = 44\%$ - 47% . The strain domain where both loading and unloading conductivities are superimposable increases with cycling by almost 0.5% to 14%. For $\epsilon_{\max} = 40.5\%$, 81%, 92% and 110% the loading and unloading conductivities coincide at a precise strain magnitude which increases with the cycling until the stabilization of conductivity (Fig. S5 from SI). This result suggests that conductivity upon loading and unloading does not necessary superimpose but can coincide in limited strain regions in which the conductive networks may be similar. As a summary, material education at $\epsilon_{\max} = 75\%$ tends to improve the electrical conductivity of CB/TPU optimally, since it increases from 0.117 S/cm up to 2.55 S/cm after 20 cycles.

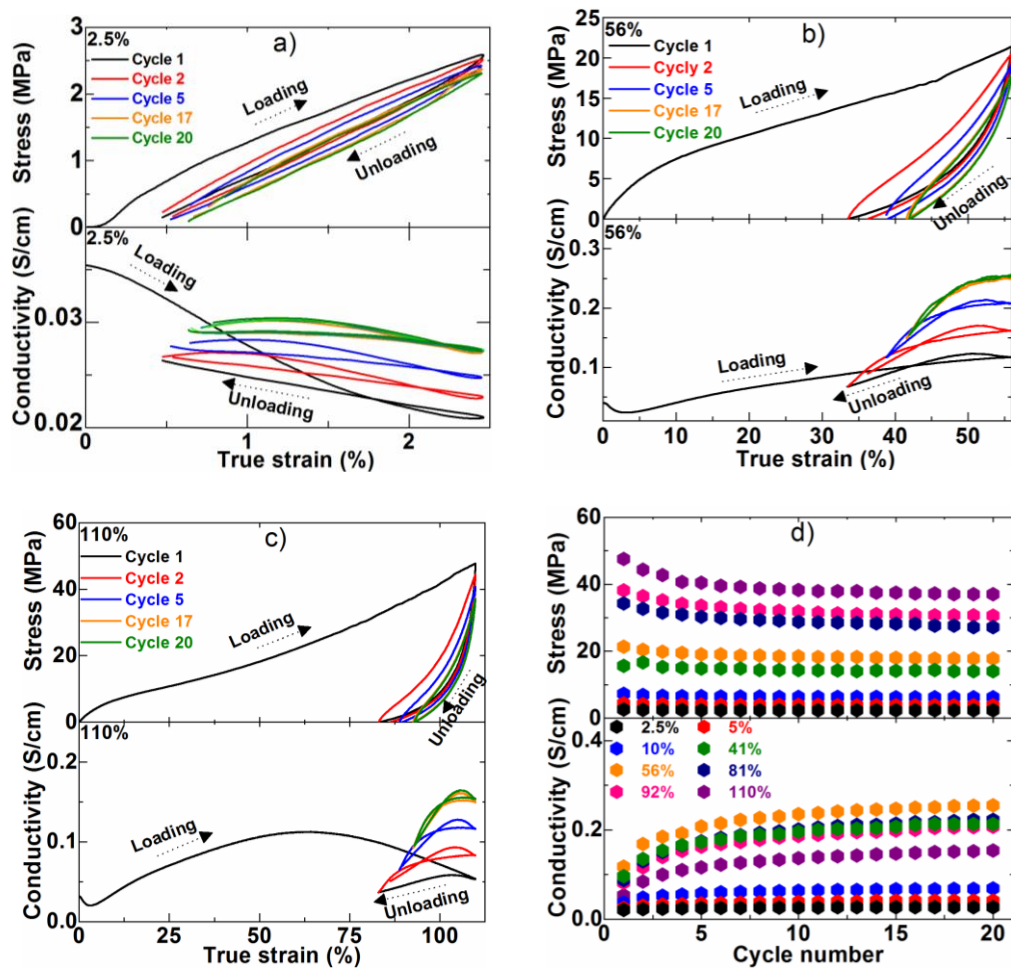


Figure 6: a) b) c) Merged graph of stress and conductivity vs strain for CB/TPU samples during 20 cyclic loading/unloading processes at a displacement rate of 10 mm/min up to ϵ_{\max} close to a) 2.5%, b) 56% and c) 110% d) Merged graph of stress and conductivity evolution at the maximum applied strain with loading/unloading cycle number.

At large ϵ_{\max} (110%), the conductivity upon loading at the 1st cycle is higher than the conductivity upon unloading, with a maximum difference of 63%. At the 2nd cycle, the conductivity upon loading is higher than that upon unloading with a maximum difference of 10% for $83\% < \epsilon < 96\%$. For $\epsilon > 96\%$, the unloading conductivity overpassed the loading value with a maximum difference of 12%. These two behaviors were evidenced for the following cycles while the strain domain in which they occurred is modified until the electrical properties became stable. As already mentioned, for ϵ_{\max} equal to 2.5% and 56%, loading/unloading cycles enhance electrical conductivity, and accordingly, the conductivity at $\epsilon_{\max} = 110\%$ increases from 0.054S/cm to 1.53 S/cm between the 1st and 20th cycles. The fillers network rearrangement occurs mostly during the 1st loading stage whereas upon unloading the polymer chains continue to relax and induce the CB displacements and connections. Since conductivity progressively evolve upon loading/unloading cycles, the viscoelastic and plastic evolution of TPU matrix may impacts the conduction channels formed by CB particles, by CB desorption from TPU, CB/CB interactions³⁸. Consequently, distinct conductivity pathways formed by CB particles are continuously explored. Boyce and Qi reported that the equilibrium behavior in neat TPU submitted to cyclic loading/unloading originates from the entropy change of long macromolecular chain portions in amorphous SD due to the orientation of the molecular network with deformation¹¹. When such equilibration of macromolecular orientation is achieved after some loading/unloading cycles, a cyclic reproducible network evolution can be obtained. In this view, change of the TPU HD/SD microstructure, possibly due to rearrangements of the phase separated structure induced by stretching may also play a role in the structuration of the conductive CB network. Thus, we are led to investigate the impact of the structural state of the TPU on the mechanical and electrical conductive effects with applied deformation.

Impact of thermal annealing on morphological, mechanical and electrical properties

In order to tackle the issue of morphological changes occurring in CB/TPU composite upon stretching and annealing, thermal investigations were carried out for neat TPU and CB/TPU composite. Thermally-induced morphological changes were achieved in both polymer matrix and CB/TPU samples by annealing them for 20 h in a wide range of annealing temperatures (T_a) from 50 °C to 175 °C, under vacuum. The annealed samples were further kept at room temperature (24 °C) for 24 h under air atmosphere and submitted to uniaxial tensile test at a strain rate of 10 mm/min. Each measurement was repeated at least three times with a fresh sample. Figure 7 illustrates the DSC thermogram of annealed CB/TPU in comparison with a non-annealed reference sample a) before and b) after uniaxial tensile test.

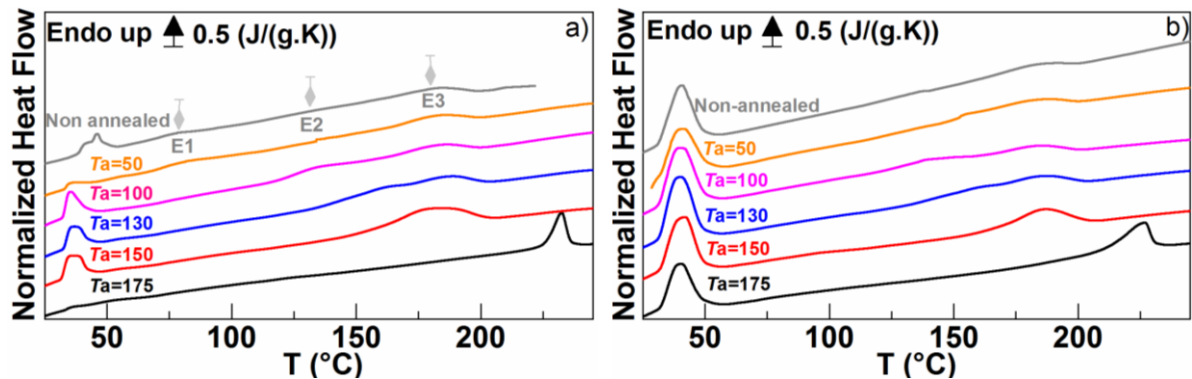


Figure 7: DSC thermograms of annealed samples and non-annealed before a) and after stretching at 10 mm/min (until failure) b), respectively

First, the intensity of the melting peak of SD depended on the annealing temperature. For non-stretched samples, the maximum melting enthalpies were obtained for annealing performed at 100 °C, 130 °C and 150 °C with similar enthalpies of 3.2 J/g, 3.85 J/g and 3.41 J/g respectively. The samples annealed at 50 °C and 175 °C presented lower enthalpies with values of 0.3 J/g and 0.17 J/g, respectively. When stretching was

applied, the melting enthalpy considerably increased for all the samples and remained dependent of annealing temperature. The melting enthalpy of SD for stretched samples was higher for annealing performed at $T_a=100^\circ\text{C}$ (13.5 J/g), $T_a=130^\circ\text{C}$ (13.8 J/g) and $T_a=150^\circ\text{C}$ (11.8 J/g) when compared to $T_a=50^\circ\text{C}$ (10 J/g) and 175°C (9 J/g). Moreover, the three endothermic peaks appearing in the thermal signal of the non-stretched and non-annealed samples and assigned as E1, E2 and E3 are impacted by the annealing process. As the annealing temperature T_a increases ($T_a \leq 150^\circ\text{C}$) the three peaks progressively merge and form a large endothermic peak after annealing at 150°C . Seymour and Cooper [8] reported that these processes are associated to the disordering of the HD segments that gained ordering during annealing. For $T_a=175^\circ\text{C}$ only a single well-defined endothermic peak was observed with an onset temperature around 225°C . This peak is associated to the melting of microcrystalline HD formed during the annealing and ordering at $T_a=175^\circ\text{C}$. Upon stretching the onset temperature decreases down to 212°C and the peak broadened. Apart from this last point, and the significant increase of the SD crystallinity, most of the features of the thermograms concerning HD were unchanged by stretching.

As previously shown from DSC analyses, annealing induces the ordering of the HD depending on the annealing temperature while stretching promotes the crystallization of the SD. The degree of ordering of HD impacts the degree of crystallization of the SD. In the following, we propose to investigate the impact of thermally induced structural ordering of the HD on the mechanical properties of CB/TPU.

Effects of annealing on mechanical properties

Figure 8 displays the true stress-strain behaviors of CB/TPU annealed at 50°C , 100°C , 130°C , 150°C and 175°C . The mechanical behavior is slightly impacted by the annealing process since singular evolution appears for each T_a . From the insert figure, one can determine the elastic modulus of the polymer backbone as previously detailed in section 2a.

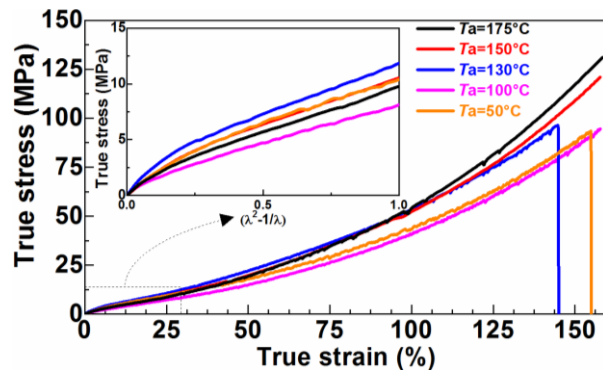


Figure 8): Stress vs strain evolution for annealed CB/TPU samples at various T_a from 50°C up to 175°C. The inset illustrates the stress evolution as function of $(\lambda^2 - 1/\lambda)$ in the small strain domain.

Table 2 presents the elastic modulus of the annealed samples from 50°C to 175°C.

Table 2: Elastic modulus values for annealed samples as calculated from equation 1

T (°C)	50	100	130	150	175
E (MPa)	25	21	28	25	25

Due to the minimal initial length of the samples and the high deformability of some of them, failure could not be observed for all the annealed samples. However, annealing at high temperature promotes higher stress at large strain ($\epsilon \geq 140\%$) compared to annealing performed at low temperature. This behavior is due to the high degree of ordering of the HD enhanced by high temperature annealing. The sample annealed at 130°C presented the highest modulus (28 Mpa) but broke at the lowest strain value (145%). This high modulus value may be attributed to the loss of flexibility of the polymer chains due to crystallization of the SD upon storage at room temperature as evidenced from the DSC data. Therefore, the annealing and storage protocol may strongly increase the stiffness of the polymer chains at $T_a=130^\circ\text{C}$

The samples annealed at 50°C, 150°C and 175°C presented the same modulus value ($E=25$ MPa) but only the annealed sample at 50°C broke at $\epsilon_R=155\%$ upon stretching. The lowest modulus value was obtained for $T_a=100^\circ\text{C}$ ($E=21$ MPa) and this sample did not break upon stretching (at the limit of the apparatus). A general trend of the modulus evolution depending on T_a could not be identified. Nevertheless these thermally induced effects on mechanical properties must be related to the HD/SD microstructural changes induced by annealing and stretching. Yanagihara and coworkers ⁶ reported that the volume fraction and the size of 4-4'-diphenylmethane diisocyanate HS-rich domain increases from 0.204 up to 0.268 with T_a (from 25°C up to 145°C), but surprisingly the elastic modulus decreases from 36.5 MPa down to 20.2 MPa. The loss of stiffness was associated to the decrease in the constraint effect of the HD on the molecular mobility of polyester glycol SD since the T_g of SD diminished for over 15°C with T_a . Nevertheless in the present PBA based-TPU, such conclusion cannot be drawn since no general trend regarding the modulus evolution with T_a was highlighted. In the following, we suggest to shed light on the structural evolution of CB/TPU after thermo-mechanical treatment by mean of WAXS analyses.

Effects of annealing on structural properties

WAXS analyses were performed in order to elucidate the structural and morphological changes occurring during annealing and extreme stretching (failure). The 2D WAXS pattern illustrated in figure 9 shows an isotropic scattering pattern, suggesting that no preferential orientation is induced by annealing at various temperatures. Nevertheless, when increasing the annealing temperature, the intensity and the smoothness of the scattering circles increase independently of the orientation.

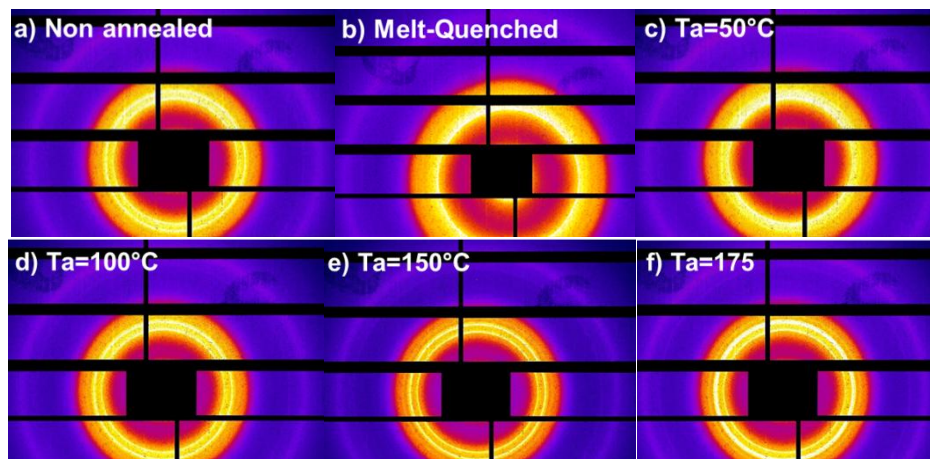


Figure 9): 2D WAXS pattern of a) non-annealed CB/TPU, b) melt-quenched and annealed samples at c) $T_a=50^\circ\text{C}$, d) $T_a=100^\circ\text{C}$, e) $T_a=150^\circ\text{C}$ and f) $T_a=175^\circ\text{C}$.

This behavior is dominated by the ordering of the HD into bigger microcrystalline domains induced by increasing T_a as previously evidenced from DSC results. It is worthy to be mentioned that the SD can also crystallize upon storage at room temperature after the annealing at $T_a \geq 50^\circ\text{C}$.

Figure 10 presents the 1D WAXS patterns of the non-annealed, melt-quenched and annealed samples at $T_a \geq 50^\circ\text{C}$ in both a) parallel and b) perpendicular to the stretching direction. Both I_{\parallel} and I_{\perp} illustrate identical scattering patterns confirming the isotropic behavior discussed above.

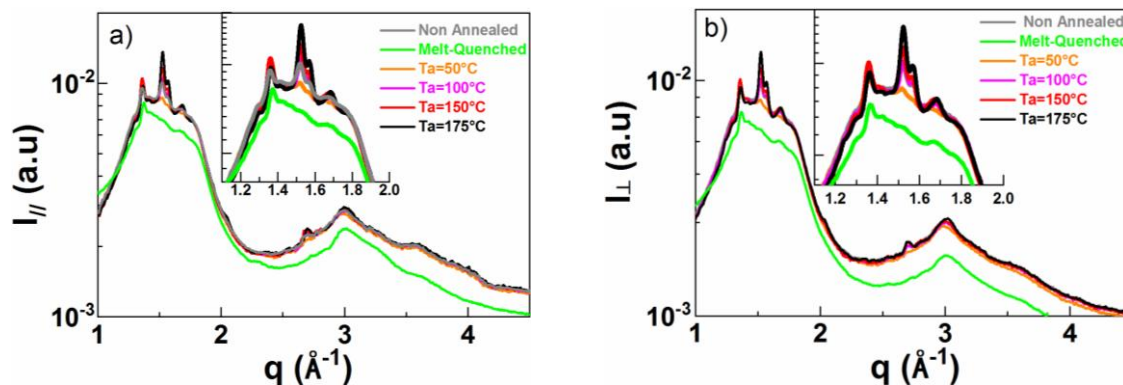


Figure 10: 1D WAXS pattern of the non-annealed, melt-quenched and annealed samples at different T_a in the direction a) parallel to the stretching direction and b) perpendicular to the stretching direction

The melt-quenched sample presented a strong amorphous halo suggesting a high amorphous ratio generated upon the melt quenching process. This result is consistent with the DSC data since no evidenced of the SD crystallization was reported but only multiple endothermic events associated to the loss ordering of the HD.

The microcrystalline HD possess fibrillar and/or lamellar morphology^{12,43}. In the fibrillar morphology, the long axes of the HD coincide with the chain direction. While in the lamellar morphology, the long axis of the HD is perpendicular to the chain direction. Stretching may induce easy orientation of the fibrillar HD long axis along the stretching direction. While in the lamellar morphology, the long axis of the HD must rotate in order to align with the chain extension⁴³.

Figure 11 presents the 2D WAXS pattern of the annealed and stretched sample (up to failure) at a cross head speed of 10 mm/min. The intensity of the scattering pattern strongly converges to the equatorial direction (perpendicular to the stretching direction) and diminishes in the meridional direction (parallel to stretching direction).

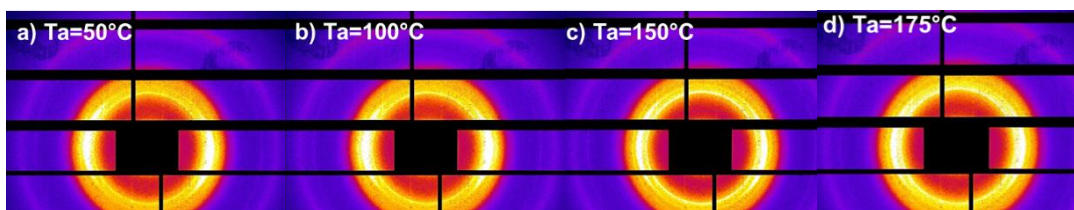


Figure 11): 2D WAX pattern of CB/TPU annealed and stretched up to failure for a) $T_a=50^\circ\text{C}$, b) $T_a=100^\circ\text{C}$, c) $T_a=150^\circ\text{C}$ and d) $T_a=175^\circ\text{C}$.

This anisotropy is clearly evidenced when plotting the 1-D WAXS pattern in both equatorial and meridional directions (figure 12). Yeh et al⁴³ suggested that this behavior is associated to the strain induced crystallization of the amorphous SD in the stretching direction. Concomitantly, the stretching of the SD induced a stress transfer toward the HD. Thus, the HD long axes may continuously rotate in order to follow the stretching direction. Liao et al⁴⁴ suggested a slipping/tilting process of the original lamellar followed by their fragmentation upon increasing strain magnitude in the case of polyethylene copolymer. At this extreme stretching, the fragmentation of the HD into small block of lamellar HD must be taken into account since the stress transfer can induce the destruction of the initial lamellar HD.

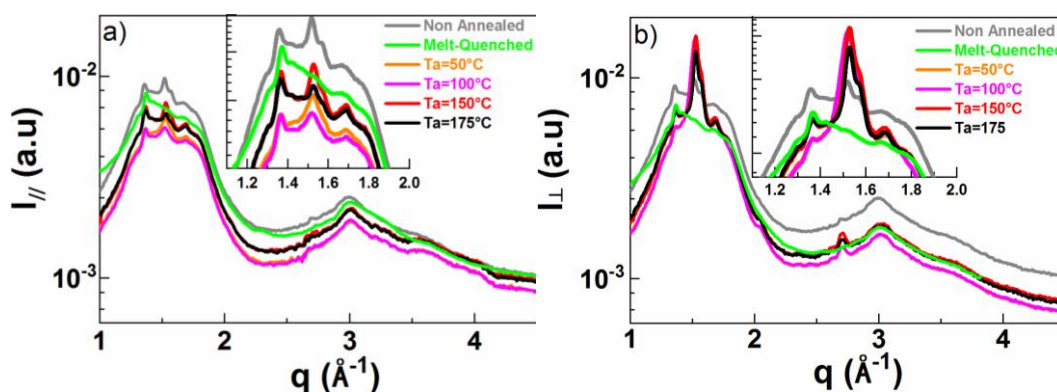


Figure 12): 1D WAXS pattern of CB/TPU annealed at different T_a and stretched up to failure recorded in both a) meridional and b) equatorial directions. The non-annealed and melt-quenched samples are added as references and were not stretched.

The overall crystalline ratio was determined from 1-D WAXS pattern, averaging azimuthally the intensity at each q value. The average scattering intensity was mathematically deconvoluted into contributions of amorphous halo (Gaussian functions) and crystalline lamellae (Lorentzian functions) and the area under each contribution permitted to evaluate the crystalline ratio. Figure 13 shows the evolution of the crystalline ratio with the annealing temperature for a) non-stretched and b) stretched samples. The crystalline ratio of the

annealed sample increases monotonically with the annealing temperature. The overall crystallinity of the annealed sample is mostly dominated by the growth of the HD depending on T_a . Extreme stretching promotes the crystallization of the SD but also the fragmentation of the HD. Considering the complexity of this feature, the overall crystallinity can be analyzed as a competition between the crystallization of the SD and the fragmentation of the HD. The crystallinity increases upon extreme stretching by 52% for $T_a=50^\circ\text{C}$ and 34% for $T_a=100^\circ\text{C}$, no significant change of the overall crystallinity was evidenced for $T_a=150^\circ\text{C}$. Nevertheless for $T_a=175^\circ\text{C}$, the crystalline ratio diminishes by 38% upon extreme stretching. From our previous hypothesis, the behavior at $T_a=175^\circ\text{C}$ is dominated by the fragmentation of the lamellar HD over the crystallization of the SD. However at $T_a=50^\circ\text{C}$ and $T_a=100^\circ\text{C}$ the overall crystallinity is dominated by a strong crystallization propensity of the SD induced by stretching over the fragmentation of the lamellar HD. In case of $T_a=150^\circ\text{C}$, the fragmentation of the HD seems to be compensate by the crystallization of the SD.

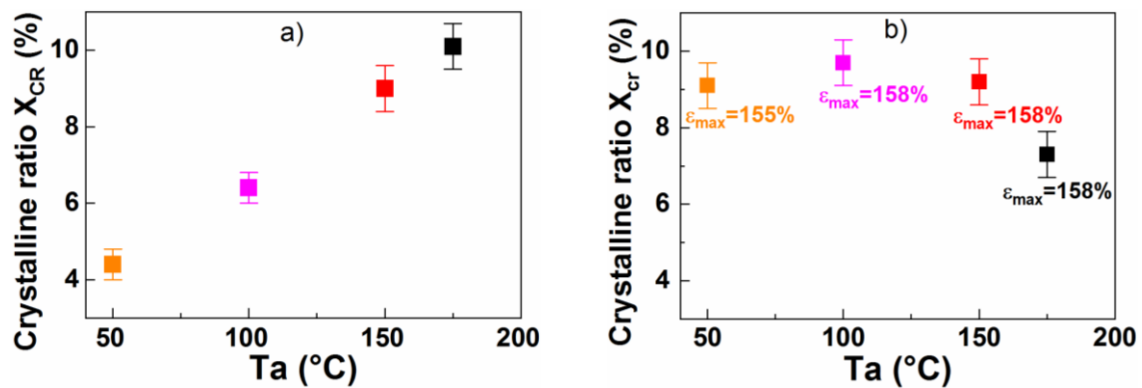


Figure 13): Overall crystalline ratio of CB/TPU annealed at different temperatures for the a) non-stretched and b) stretched samples.

The average size of the crystallites lamellae D can be calculated from the 1-D WAXS intensity distribution curve (azimuthally average at each q value) using the Scherrer equation:

$$D = \frac{k\lambda}{\beta \cos\theta} \quad (3)$$

Where $k=0.9$ is the crystalline shape factor, $\lambda = 0.78968 \text{ \AA}$ is the wavelength of the X-ray, β the full-width at half-maximum (FWHM) in radians and 2θ the scattering angle. Table 3 resumes the crystallites sizes of the annealed/non stretched and annealed/stretched samples determined by evaluating the FWHM of the most intense peaks located at $q=1.36 \text{ \AA}$ and $q=1.52 \text{ \AA}$.

Table 3: Size of the crystallites depending on T_a and stretching

T (°C)	50	100	150	175
D_{non-stretched} (nm)	9.9	13.5	15.2	16.8
D_{stretched} (nm)	6.5	7	13.0	13.2

The size of the crystalline lamellae increases with temperature from 9.9 nm at $T_a=50^\circ\text{C}$ up to 16.8 nm at $T_a=175^\circ\text{C}$ independently of the orientation. Unfortunately, stretching induces an anisotropic fragmentation of the lamellae reducing their size.

Up to now, we were focused on the structural evolution of the polymer matrix thermo-mechanically induced without mentioning their impact on the arrangement of the CB fillers. In the following we propose to tackle this issue.

Effects of annealing and stretching on electrical properties

After evaluating the impact of annealing on mechanical properties of CB/TPU we now propose to evaluate the impact of annealing on electrical conduction properties. Figure 9 depicts the conductivity evolution with strain of annealed sample at 50°C, 100°C, 130°C, 150°C and 175°C for 20h and stored 24h at 24°C. In contrast to the mechanical properties, the conductivity-strain behavior seems to be highly impacted by annealing. The three conduction regimes previously reported for non-annealed samples persisted for annealed samples from $T_a=50^\circ\text{C}$ up to $T_a=150^\circ\text{C}$, whereas the sample annealed at 175°C shows a continuous decrease of conductivity upon stretching. Interestingly, the conductivity maximum increases from 0.122 S/cm to 0.164 S/cm when varying T_a from 50°C to 100°C and diminishes from 0.154 S/cm to 0.087 S/cm as T_a increases from 130°C to 150°C . Furthermore, the increase of conductivity occurs for strains below 58%, 55% and 60% for $T_a=50^\circ\text{C}$, $T_a=130^\circ\text{C}$ and $T_a=150^\circ\text{C}$, respectively. While for $T_a=100^\circ\text{C}$, the increase of conductivity occurs at very large strain domain (90%) with the maximum conductivity obtained for $\varepsilon=92\%$. Therefore, annealing at 100°C was the optimum condition for conductivity enhancement. The annealing may favors the establishment of highly conductive pathways resistant to strain alteration. Annealing carried out at $T_a=175^\circ\text{C}$ apparently leads to a polymer SD/HD morphology that does not promote the conductivity channels establishment, possibly with dominant fragmentation of the conductive network by uniaxial stretching.

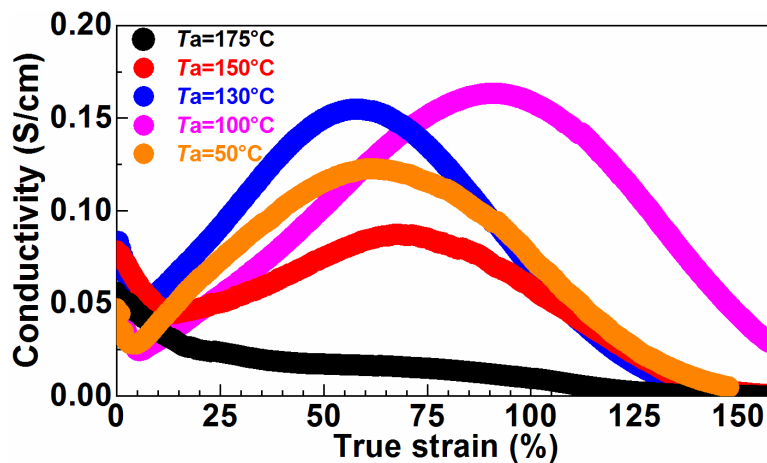


Figure 14: Conductivity vs Strain evolution for annealed CB/TPU samples at various T_a from 50°C up to 175°C at a crosshead speed of 10 mm/min.

SAXS analysis

The scattering region covers by our SAXS measurements ($0.00675 \text{ \AA}^{-1} \leq q \leq 0.4 \text{ \AA}^{-1}$) allow to investigate the interfacial structure between the polymer and the CB fillers, the size and distributions of primary CB particles and those of CB aggregates less than 100 nm. The scattering intensities in the equatorial (I_{\perp}) and meridional directions (I_{\parallel}) over the range $0.00675 \text{ \AA}^{-1} \leq q \leq 0.15 \text{ \AA}^{-1}$ are displayed in figure 15. The $I(q)$ vs q feature plotted on the log-log scale can be described by a power-law given by: $I(q) \sim q^p$ where p is the exponent of the power-law. When plotting $I(q)$ vs q in the log-log scale, p value is calculated from the slope of the curve. Depending on the q region, p value may give morphological information about the CB fillers and their state of aggregation⁴⁵⁻⁴⁷.

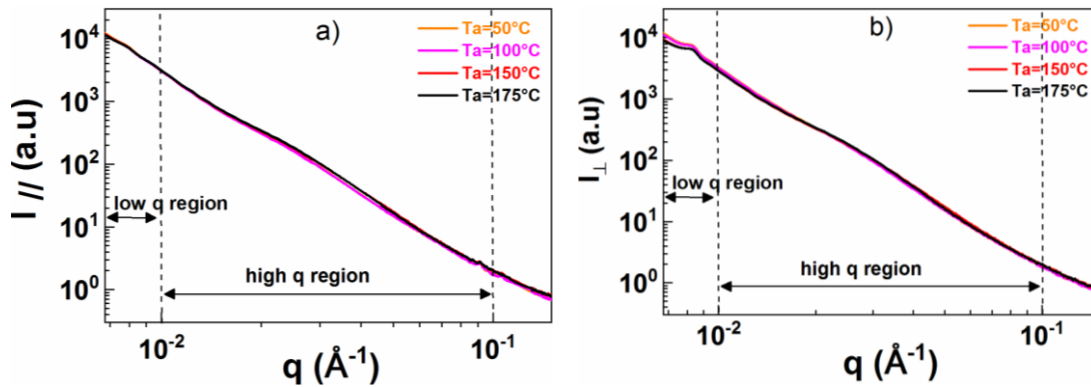


Figure 15: log-log plot of $I(q)$ vs q in both a) meridional and b) equatorial directions for annealed and stretched samples

At low q range ($q \leq 0.02 \text{ \AA}^{-1}$), the power-law is characteristic of aggregated CB primary particles ($\leq 100 \text{ nm}$)⁴⁵. The evolution of exponent p may therefore indicate the degree of interpenetration of the CB aggregates in both meridional and equatorial axes. The exponent parameters derived from the log-log plots of $I(q)$ vs q in the meridional and equatorial directions are resumed in table 4 and 5 respectively.

Table 4: Power law exponent for the scattering intensity in the meridional direction

T (°C)	50	100	150	175
Low q power exponent	-3.5	-3.5	-3.5	-3.4
High q power exponent	-3.2	-3.2	-3.3	-3.3

Table 5: Power law exponents for the scattering intensity in the equatorial direction

T (°C)	50	100	150	175
Low q power exponent	-3.2	-3.2	-3.0	-2.9
High q power exponent	-3.3	-3.3	-3.2	-3.2

The absolute value of the exponent is higher in meridional direction compared to its value in the equatorial direction for all T_a . This suggests an interpenetration of CB primary particles in the equatorial direction while in the stretching direction the degree of interpenetration of the CB aggregates decreases. This behavior is consistent with idea of depercolation in the meridional direction since the distance between neighboring CB particles increases along the stretching direction. Interestingly, in the equatorial direction, higher degree of CB particles interpenetration occurs at 150°C and 175°C. At first glance, this feature seems to be contradictory

with the evolution of conductivity for both Ta since they possess lower gain of conductivity upon stretching. In fact, even though CB aggregation is pronounced in the direction perpendicular to stretching at 175°C and 150°C, these CB aggregates need interconnections between them to enhanced conduction channels. Unfortunately, these interconnections were not guarantee by the amorphous flow of the SD.

In the q region $0.02 \leq q (\text{\AA}^{-1}) \leq 0.1$, the exponent parameter $p \sim -3.3$ is almost the same in both directions independently from Ta. In this q region the exponent parameter p gives the surface characteristics of the primary CB particles⁴⁵⁻⁴⁷. The value of -3.3 suggests that the surface of the CB particles is rough are characterize by surface fractals. Thus, neither the annealing nor the stretching modified the surface of the primary CB particles. From all these observations, we propose to draw the following conclusions regarding the evolution of the matrix and the fillers upon thermo-mechanical solicitation:

(a) Annealing enhances morphological changes of both SD and HD and continuous formation of short-range ordered HD. Moreover severe annealing (175°C) promotes the transition from short-range ordered into microcrystalline HD.

(b) Stretching amplifies the crystallization of the SD but can decrease the ordering of the microcrystalline HD.

As illustrated in figure 16, the melting enthalpy of the SD and the maximum conductivity measured at the crosshead speed of 10 mm/min are highly correlated. The highest conductivity values were obtained for samples annealed at 100°C and 130°C. Interestingly, these samples contained the highest crystallized SD ratio. Nonetheless, the lowest conductivity value was obtained for Ta=175°C (0.0125 S/cm) even though such a thermal treatment yields a HD morphology with high ordering. As a result, strain induced crystallization of the SD enhances the formation of conductivity channels, while the ordering of the HD into microcrystalline structure plays a minor role on conductivity. Annealing at Ta≥50°C induces melting of the SD and morphological changes of the HD. When increasing the annealing temperature Ta from 50°C up to 175°C the HD can be strongly ordered and crystalize. When storing the annealed sample at room temperature, the SD can undergo crystallization, depending on Ta. At high annealing close to 175°C, very few amount of the SD undergoes crystallization possibly resulting from constraints effects from the crystallized HD.

This HD-reinforced morphology results in higher strength and higher strain at break. Nevertheless, the conductivity of samples annealed at $T_a \geq 150^\circ\text{C}$ drastically diminishes upon stretching since the CB fillers are located in amorphous SD that did not ensure the interconnection among the CB aggregates. For lower T_a values, the constraint effect of the crystallized HD on the SD diminishes and higher SD fraction can undergo crystallization upon storage at room temperature, and the overall crystallinity ratio is increased by stretching. Consequently, from this local concentration effect of CB in the remaining amorphous phase, suitable conductivity pathways are formed upon stretching.

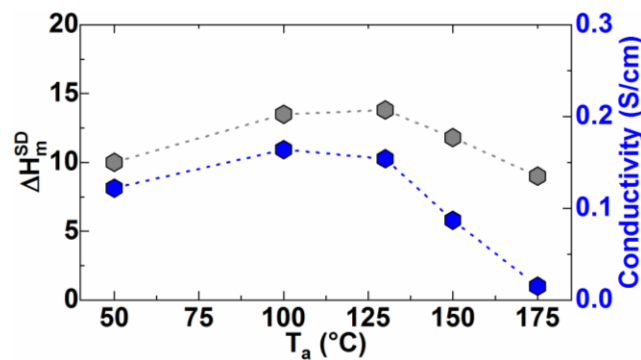


Figure 16: Evolution of the SD melting enthalpy and maximum conductivity as function of T_a for CB/TPU.

Impact of strain rate on morphology

Figure 17a) depicts the thermal signature of CB/TPU filaments submitted to various strain rates and analyzed postmortem and compared with a non-stretched sample. The non-stretched sample presented complex endothermic events in the melting region of the SD. At $T > 50^\circ\text{C}$ the endothermic peaks are generally associated to the loss of short and long range order in the HD^{13,14}. For the stretched samples, various thermal events occurred during heating. The endothermic peak observed at $32^\circ\text{C} \pm 1^\circ\text{C}$ is associated to the melting of the crystallized SD. At $T > 50^\circ\text{C}$, morphological changes of HD occur are known to^{13,14} but no significant differences were evidenced when increasing the strain rate. As illustrated in figure 11b the melting enthalpy of

the SD decreases from 14 J/g to 8.5 J/g and the maximum conductivity from 0.25 S/cm to 0.095 S/cm with increasing crosshead speed. This confirms that the SD undergoes crystallization upon stretching. Since crystallization is a kinetic process, stretching at low strain rate may allow the formation of a higher crystallized fraction of the SD than stretching at high strain rates. Moreover, the melting enthalpy of SD domains and the maximum conductivity of CB/TPU are closely related. These results may suggest that the changes occurring in the electrical properties of TPU/CB are mostly governed by the structural crystalline changes occurring in the SD rather than in the HD.

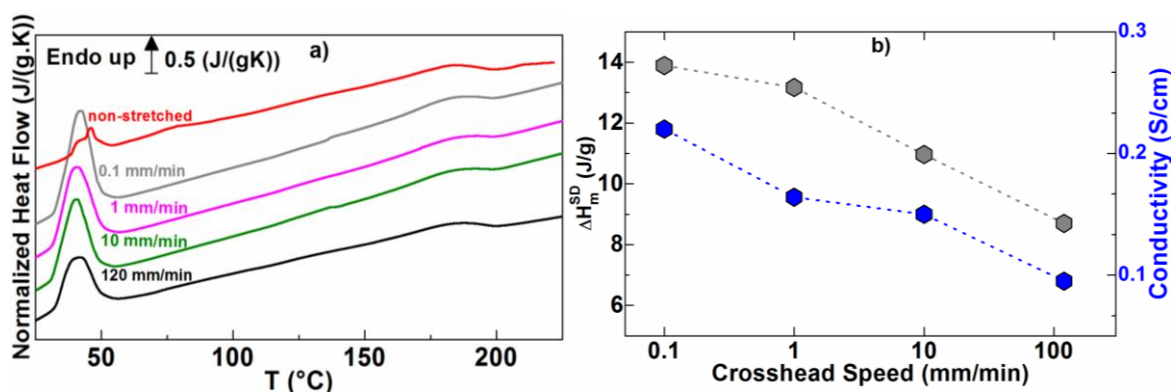


Figure 17: a) DSC thermogram of CB/TPU submitted to various strain rate from 0.1 up to 120 mm/min b) Evolution of the melting enthalpy of the soft segments (in gray) and maximum conductivity (in blue) as a function of strain rate.

The morphology and the size analyses of the CB aggregates and the perimeters of CB free domains are displayed in the supplementary information (section S5) for non-stretched CB/TPU. Figure 18 illustrates the TEM images of the samples stretched at 120 mm/min and 0.1 mm/min at a scale bar of 1 μ m.

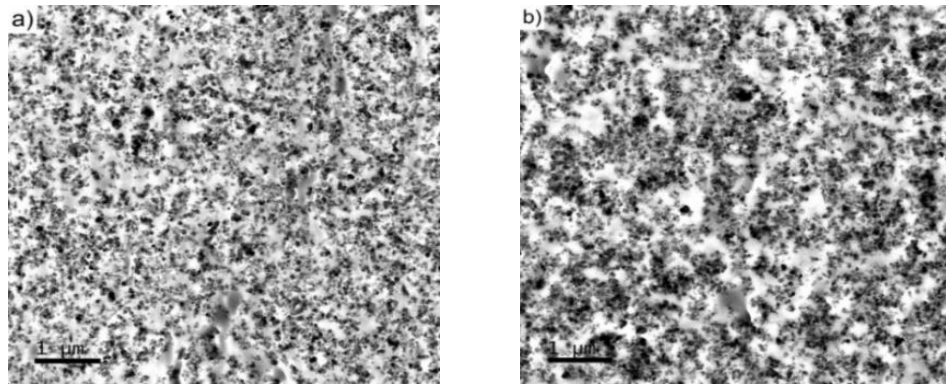


Figure 18: TEM image of the stretched sample at a) 120 mm/min and b) 0.1 mm/min with a bar scale of 1 μm .

The sample stretched at high strain rate (120 mm/min) showed a more homogeneous dispersion of CB fillers within the polymer matrix compared to slow stretching (0.1 mm/min). Both stretched composites were formed of isolated, small medium and large aggregated CB particles and few regions were bared of CB. However, slow stretching (0.1 mm/min) promotes large size aggregated CB fillers, large domains free of CB and CB interpenetration. Figure 19 shows the double log plot of the frequency of occurrence for domains denuded of CB with distinct surface area for stretched samples at a) 120 mm/min and b) 0.1 mm/min. The perimeters of the CB bared domains are presented for stretching performed at a') 120 mm/min and b') 0.1 mm/min. For the sample stretched at the highest strain rate (120 mm/min), almost 90% of the domains free of CB are of type A1 ($10^{-6} \leq A1 (\mu\text{m}^2) < 10^{-5}$) and A2 ($10^{-5} \leq A2 (\mu\text{m}^2) < 10^{-4}$) and only 10% are of type A3 ($10^{-4} \leq A3 (\mu\text{m}^2) < 10^{-3}$) and A4 ($10^{-3} \leq A4 (\mu\text{m}^2) < 10^{-2}$). None of them possess a surface area $\geq 10^{-2} \mu\text{m}^2$. Moreover, the perimeters of the CB bared domains are for 98% $< 0.8 \mu\text{m}$ and less than 1% is of type P4 ($1.6 \leq P4 (\mu\text{m}) < 8$). These results are consistent with the homogeneous dispersion of CB within the matrix and the low tendency of CB aggregation upon high speed stretching. However, the sample stretched at the lowest stretching rate (0.1 mm/min) presented a higher occurrence of large size domains free of CB (around 19% of occurrence) with nearly 2% of domains with a surface area $\geq 10^{-2} \mu\text{m}^2$. This value is even higher compared to the non-stretched sample. Furthermore, the perimeters of the CB free domains are for almost 90% $< 0.8 \mu\text{m}$ and 4.5% are of type P4 (1.6

$\leq P4 (\mu\text{m}) < 8$). Thus, these results are consistent with the heterogeneous dispersion of CB particles within the matrix and the formation of large size domains of aggregated CB. From all of these observations, it was clear that stretching highly impacted the dispersion of CB fillers in the polymer matrix. As reported in the previous sections, stretching promoted the crystallization of the amorphous SD, amplified by slow stretching. As crystallization occurred, the CB fillers initially dispersed in the amorphous SD, are expelled from the crystalline SD and confined in residual continuous amorphous SD increasing the local CB concentration highly above the percolation threshold.

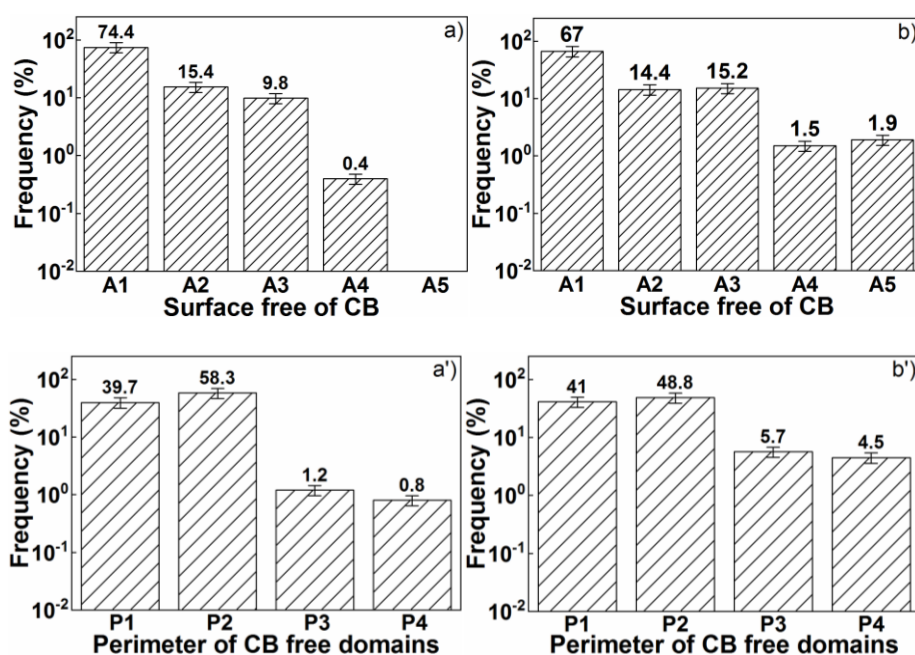


Figure 19: (a-b) Double log plot of frequency of occurrence for surface areas free of CB with different sizes ($10^{-6} \leq A1 (\mu\text{m}^2) < 10^{-5}$, $10^{-5} \leq A2 (\mu\text{m}^2) < 10^{-4}$, $10^{-4} \leq A3 (\mu\text{m}^2) < 10^{-3}$, $10^{-3} \leq A4 (\mu\text{m}^2) < 10^{-2}$, $10^{-2} \leq A5 (\mu\text{m}^2) < 10^{-1}$) for stretched samples at a) 120mm/min and b) 0.1 mm/min. (a'-b') Double log plot of frequency of occurrence of domains free of CB with various perimeters ($0.08 \leq P1 (\mu\text{m}) < 0.16$, $0.16 \leq P2 (\mu\text{m}) < 0.8$, $0.8 \leq P3 (\mu\text{m}) < 1.6$, $1.6 \leq P4 (\mu\text{m}) < 8$) for stretched samples at a') 120mm/min and b) 0.1 mm/min.

Figure 20 presents the double log plot of $I(q)$ vs q in both parallel and perpendicular to the stretching direction of samples stretched at 0.1 and 120 mm/min. As mentioned previously this representation permits to study the CB aggregates interpretation (at low q region) in both direction and the nature of the surface of primary CB particles (at high q region).

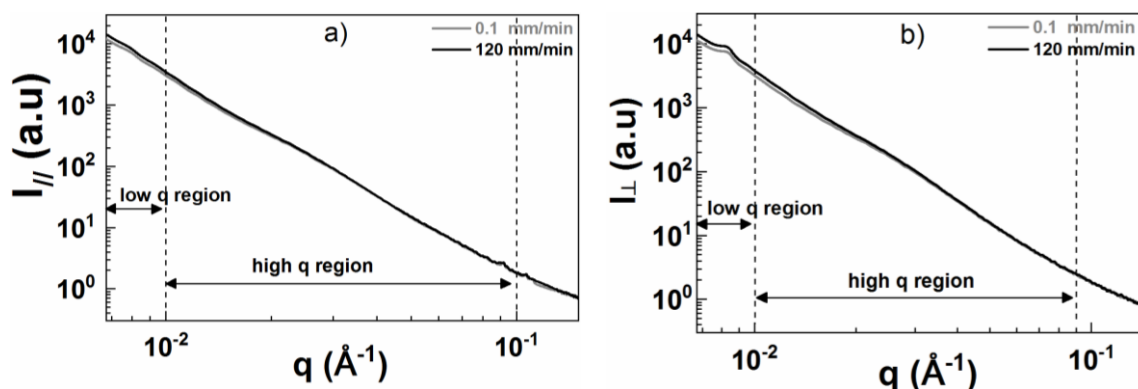


Figure 20: log-log plot of $I(q)$ vs q in the a) meridional and b) equatorial directions of samples stretched at 0.1 and 120 mm/min

The strain rate dependency of the power law ($I(q) \sim q^p$) exponent is resumed in table 6 and 7 for both meridional and equatorial directions. In the low q region, the exponent increases with decreasing strain rate in both directions. Additionally, at the same strain rate, the exponent parameter strongly increases in the equatorial direction. Suggesting that stretching at low strain rate may enhance CB aggregates interpenetration mostly in the direction perpendicular to stretching. While in the stretching direction disentanglement of CB aggregates may dominate. This interpretation is consistent with the high conductivity value at low strain rate.

Table 6: Power law exponents for the scattering intensity in the meridional direction

Cross head speed mm/min	0.1	120
Low q power exponent	-3.4	-3.6
High q power exponent	-3.3	-3.3

Table 7: Power law exponents for the scattering intensity in the equatorial direction

Cross head speed mm/min	0.1	120
Low q power exponent	-2.8	-3.0
High q power exponent	-3.3	-3.3

Generally, the electrical and mechanical properties of conductive composites are directly tuned during the formulation step and mostly governed by the choice of the polymer matrix and the filler ^{48,49}. We therefore proposed an original approach to tune advantageously both mechanical and electrical properties by a thermo-mechanical treatment inducing structural modifications within the polymer matrix impacting the percolation threshold.

4. Conclusions

In the present study, in-situ coupled mechanical/electrical investigations on TPU/CB composite were carried-out under continuous and cyclic mechanical loading, with simultaneous measurements of stress, strain and electrical conductivity in dependence on the strain rate and amplitude. Our study highlights the role played by morphological changes induced by uniaxial tensile stress and/or thermal annealing in the TPU matrix on the electromechanical coupling of conductive TPU/CB composites. These morphological changes are intimately

related to the behavior of the soft and hard domains. Upon stretching, the soft domains (SD) undergo crystallization while no significant changes are reported for the HD. The crystallization behavior of the SD is highly sensitive to the strain rate. Slow stretching promotes high crystallization fraction of the SD. The higher the stretching rate the lower will be the crystallized fraction of the SD. Crystallization of the SD increases the elastic modulus of the composite which also becomes more brittle. Upon stretching, the electrical properties evolve according to three regimes, described as follows: (i) Subtle decrease of the conductivity due to the perturbation of contact points of the existing conductivity channels at weak elongation. (ii) Strong increase of conductivity for almost one decade due to the creation of suitable conductivity pathways at medium elongation. (iii) Decrease of the conductivity due to the predominance of the destruction of conductivity channels over their creation at extreme elongation. Interestingly, the highest conductivity value upon stretching (0.25 S/cm) was obtained for the lowest strain rate 0.1 mm/min. This evolution is due to the fact that slow stretching promotes ordering and crystallization of SD. Thus, the crystallization of the SD enhances the formation of suitable conduction pathways by localizing the filler in the amorphous inter-crystalline zones of the SD. While stretching enhanced the crystallization of SD, the hard domains (HD) were less sensitive to deformation but strongly sensitive to thermal annealing. Annealing at $T_a \geq 50^\circ\text{C}$ promoted gradual ordering of the HD that influenced the crystallization of the SD depending on T_a . Annealing performed at 100°C and 130°C were the optimum thermal treatment conditions for intermediate HD ordering, still permitting crystallization of the SD. Annealing performed at higher temperature (175°C) enhanced the formation of long range ordered HD but frustrated the crystallization of the amorphous SD upon stretching. The partial crystallization of the SD resulted in a local concentration of CB fillers (in residual amorphous SD) above the percolation threshold and led to stable conductive channels with higher conduction properties. Both SD and HD play typically different roles in the composite. While the SD controls the flexibility of the matrix and the arrangement of the CB particles, the HD and their interactions with the SD ensure the resistance to rupture. Structural and morphological reorganizations induced by mechanical deformation and thermal treatment can be thus efficiently used to

adjust the coupled electro-mechanical behavior of TPU-based composite materials, with potential applications in the field of smart polymer-based composite materials.

4. Acknowledgments

The authors are grateful to Auvergne Rhône-Alpes region for the financial support of this work and all the collaborators of the FUI project FILOGRAPH. The help of Laurent Cavetier in fabricating some additional metallic elements necessary for the measurements cells is kindly acknowledged.

References

- (1) Akindoyo, J. O.; Beg, M. D. H.; Ghazali, S.; Islam, M. R.; Jeyaratnam, N.; Yuvaraj, A. R. Polyurethane Types, Synthesis and Applications – a Review. *RSC Adv.* **2016**, *6* (115), 114453–114482. <https://doi.org/10.1039/C6RA14525F>.
- (2) Qin, X.; Wang, B.; Zhang, X.; Shi, Y.; Ye, S.; Feng, Y.; Liu, C.; Shen, C. Superelastic and Durable Hierarchical Porous Thermoplastic Polyurethane Monolith with Excellent Hydrophobicity for Highly Efficient Oil/Water Separation. *Ind. Eng. Chem. Res.* **2019**, *58* (44), 20291–20299. <https://doi.org/10.1021/acs.iecr.9b03717>.
- (3) Hu, S.; Shou, T.; Guo, M.; Wang, R.; Wang, J.; Tian, H.; Qin, X.; Zhao, X.; Zhang, L. Fabrication of New Thermoplastic Polyurethane Elastomers with High Heat Resistance for 3D Printing Derived from 3,3-Dimethyl-4,4'-Diphenyl Diisocyanate. *Ind. Eng. Chem. Res.* **2020**, *59* (22), 10476–10482. <https://doi.org/10.1021/acs.iecr.0c01101>.
- (4) Pichon, P. G.; David, L.; Méchin, F.; Sautereau, H. Morphologies of Cross-Linked Segmented Polyurethanes. Evolution during Maturation and Consequences on Elastic Properties and Thermal Compressive Fatigue. *Macromolecules* **2010**, *43* (4), 1888–1900. <https://doi.org/10.1021/ma901602y>.
- (5) Yoon, P. J.; Han, C. D. Effect of Thermal History on the Rheological Behavior of Thermoplastic Polyurethanes. *Macromolecules* **2000**, *33* (6), 2171–2183. <https://doi.org/10.1021/ma991741r>.
- (6) Yanagihara, Y.; Osaka, N.; Iimori, S.; Murayama, S.; Saito, H. Relationship between Modulus and Structure of Annealed Thermoplastic Polyurethane. *Mater. Today Commun.* **2015**, *2*, e9–e15. <https://doi.org/10.1016/j.mtcomm.2014.10.001>.
- (7) Liu, Y.; Liu, L.; Liang, Y. Relationship between Structure and Dynamic Mechanical Properties of Thermoplastic Polyurethane Elastomer Containing Bi-Soft Segment. *J. Appl. Polym. Sci.* **2020**, *137* (45), 49414. <https://doi.org/10.1002/app.49414>.
- (8) Xiang, D.; He, J.; Cui, T.; Liu, L.; Shi, Q. S.; Ma, L. C.; Liang, Y. Multiphase Structure and Electromechanical Behaviors of Aliphatic Polyurethane Elastomers. *Macromolecules* **2018**, *51* (16), 6369–6379. <https://doi.org/10.1021/acs.macromol.8b01171>.
- (9) Seymour, R. W.; Cooper, S. L. Thermal Analysis of Polyurethane Block Polymers. *Macromolecules* **1973**, *6* (1), 48–53. <https://doi.org/10.1021/ma60031a008>.

- (10) Bueno-Ferrer, C.; Hablot, E.; Garrigós, M.; Bocchini, S.; Avérous, L.; Jimenez, A. Relationship between Morphology, Properties and Degradation Parameters of Novative Biobased Thermoplastic Polyurethanes Obtained from Dimer Fatty Acids. *Polym. Degrad. Stab.* **2012**, *97*, 1964–1969. <https://doi.org/10.1016/j.polymdegradstab.2012.03.002>.
- (11) Qi, H. J.; Boyce, M. C. Stress–Strain Behavior of Thermoplastic Polyurethanes. *Mech. Mater.* **2005**, *37* (8), 817–839. <https://doi.org/10.1016/j.mechmat.2004.08.001>.
- (12) Koerner, H.; Kelley, J. J.; Vaia, R. A. Transient Microstructure of Low Hard Segment Thermoplastic Polyurethane under Uniaxial Deformation. *Macromolecules* **2008**, *41* (13), 4709–4716. <https://doi.org/10.1021/ma800306z>.
- (13) Aurilia, M.; Piscitelli, F.; Sorrentino, L.; Lavorgna, M.; Iannace, S. Detailed Analysis of Dynamic Mechanical Properties of TPU Nanocomposite: The Role of the Interfaces. *Eur. Polym. J.* **2011**, *47* (5), 925–936. <https://doi.org/10.1016/j.eurpolymj.2011.01.005>.
- (14) Saiani, A.; Novak, A.; Rodier, L.; Eeckhaut, G.; Leenslag, J.-W.; Higgins, J. S. Origin of Multiple Melting Endotherms in a High Hard Block Content Polyurethane: Effect of Annealing Temperature. *Macromolecules* **2007**, *40* (20), 7252–7262. <https://doi.org/10.1021/ma070332p>.
- (15) Lin, L.; Liu, S.; Zhang, Q.; Li, X.; Ji, M.; Deng, H.; Fu, Q. Towards Tunable Sensitivity of Electrical Property to Strain for Conductive Polymer Composites Based on Thermoplastic Elastomer. *ACS Appl. Mater. Interfaces* **2013**, *5* (12), 5815–5824. <https://doi.org/10.1021/am401402x>.
- (16) Liu, H.; Gao, J.; Huang, W.; Dai, K.; Zheng, G.; Liu, C.; Shen, C.; Yan, X.; Guo, J.; Guo, Z. Electrically Conductive Strain Sensing Polyurethane Nanocomposites with Synergistic Carbon Nanotubes and Graphene Bifillers. *Nanoscale* **2016**, *8* (26), 12977–12989. <https://doi.org/10.1039/C6NR02216B>.
- (17) Zheng, Y.; Li, Y.; Dai, K.; Liu, M.; Zhou, K.; Zheng, G.; Liu, C.; Shen, C. Conductive Thermoplastic Polyurethane Composites with Tunable Piezoresistivity by Modulating the Filler Dimensionality for Flexible Strain Sensors. *Compos. Part Appl. Sci. Manuf.* **2017**, *101*, 41–49. <https://doi.org/10.1016/j.compositesa.2017.06.003>.
- (18) Li, H.; Yuan, D.; Li, P.; He, C. High Conductive and Mechanical Robust Carbon Nanotubes/Waterborne Polyurethane Composite Films for Efficient Electromagnetic Interference Shielding. *Compos. Part Appl. Sci. Manuf.* **2019**, *121*, 411–417. <https://doi.org/10.1016/j.compositesa.2019.04.003>.
- (19) Wang, X.; Liu, X.; Schubert, D. W. Highly Sensitive Ultrathin Flexible Thermoplastic Polyurethane/Carbon Black Fibrous Film Strain Sensor with Adjustable Scaffold Networks. *Nano-Micro Lett.* **2021**, *13*, 64. <https://doi.org/10.1007/s40820-021-00592-9>.
- (20) Zhang, S.; Wang, S.; Wang, Y.; Fan, X.; Ding, L.; Xuan, S.; Gong, X. Conductive Shear Thickening Gel/Polyurethane Sponge: A Flexible Human Motion Detection Sensor with Excellent Safeguarding Performance. *Compos. Part Appl. Sci. Manuf.* **2018**, *112*, 197–206. <https://doi.org/10.1016/j.compositesa.2018.06.007>.
- (21) Tong, L.; Wang, X.-X.; He, X.-X.; Nie, G.-D.; Zhang, J.; Zhang, B.; Guo, W.-Z.; Long, Y.-Z. Electrically Conductive TPU Nanofibrous Composite with High Stretchability for Flexible Strain Sensor. *Nanoscale Res. Lett.* **2018**, *13* (1), 86. <https://doi.org/10.1186/s11671-018-2499-0>.
- (22) Bilotti, E.; Zhang, R.; Deng, H.; Baxendale, M.; Peijs, T. Fabrication and Property Prediction of Conductive and Strain Sensing TPU/CNT Nanocomposite Fibres. *J. Mater. Chem.* **2010**, *20* (42), 9449–9455. <https://doi.org/10.1039/C0JM01827A>.

- (23) Kim, K.; Park, J.; Suh, J.; Kim, M.; Jeong, Y.; Park, I. 3D Printing of Multiaxial Force Sensors Using Carbon Nanotube (CNT)/Thermoplastic Polyurethane (TPU) Filaments. *Sens. Actuators Phys.* **2017**, *263*, 493–500. <https://doi.org/10.1016/j.sna.2017.07.020>.
- (24) Bilotti, E.; Zhang, H.; Deng, H.; Zhang, R.; Fu, Q.; Peijs, T. Controlling the Dynamic Percolation of Carbon Nanotube Based Conductive Polymer Composites by Addition of Secondary Nanofillers: The Effect on Electrical Conductivity and Tuneable Sensing Behaviour. *Compos. Sci. Technol.* **2013**, *74*, 85–90. <https://doi.org/10.1016/j.compscitech.2012.10.008>.
- (25) Dong, M.; Li, Q.; Liu, H.; Liu, C.; Wujcik, E. K.; Shao, Q.; Ding, T.; Mai, X.; Shen, C.; Guo, Z. Thermoplastic Polyurethane-Carbon Black Nanocomposite Coating: Fabrication and Solid Particle Erosion Resistance. *Polymer* **2018**, *158*, 381–390. <https://doi.org/10.1016/j.polymer.2018.11.003>.
- (26) Lin, L.; Liu, S.; Zhang, Q.; Li, X.; Ji, M.; Deng, H.; Fu, Q. Towards Tunable Sensitivity of Electrical Property to Strain for Conductive Polymer Composites Based on Thermoplastic Elastomer. *ACS Appl. Mater. Interfaces* **2013**, *5* (12), 5815–5824. <https://doi.org/10.1021/am401402x>.
- (27) Scripting the Trainable Weka Segmentation <https://imagej.github.io/plugins/tws/scripting> (accessed 2021 -07 -22).
- (28) Flandin, L.; Hiltner, A.; Baer, E. Interrelationships between Electrical and Mechanical Properties of a Carbon Black-Filled Ethylene–Octene Elastomer. *Polymer* **2001**, *42* (2), 827–838. [https://doi.org/10.1016/S0032-3861\(00\)00324-4](https://doi.org/10.1016/S0032-3861(00)00324-4).
- (29) Stricher, A. M.; Rinaldi, R. G.; Barrès, C.; Ganachaud, F.; Chazeau, L. How I Met Your Elastomers: From Network Topology to Mechanical Behaviours of Conventional Silicone Materials. *RSC Adv.* **2015**, *5* (66), 53713–53725. <https://doi.org/10.1039/C5RA06965C>.
- (30) Hussein, M. Effects of Strain Rate and Temperature on the Mechanical Behavior of Carbon Black Reinforced Elastomers Based on Butyl Rubber and High Molecular Weight Polyethylene. *Results Phys.* **2018**, *9*, 511–517. <https://doi.org/10.1016/j.rinp.2018.02.043>.
- (31) Moghim, M. H.; Zebarjad, S. M. Effect of Strain Rate on Tensile Properties of Polyurethane/(Multiwalled Carbon Nanotube) Nanocomposite. *J. Vinyl Addit. Technol.* **2016**, *22* (3), 356–361. <https://doi.org/10.1002/vnl.21452>.
- (32) Nurul Fazita, M. R.; Abdul Khalil, H. P. S.; Nor Amira Izzati, A.; Rizal, S. 3 - Effects of Strain Rate on Failure Mechanisms and Energy Absorption in Polymer Composites. In *Failure Analysis in Biocomposites, Fibre-Reinforced Composites and Hybrid Composites*; Jawaid, M., Thariq, M., Saba, N., Eds.; Woodhead Publishing Series in Composites Science and Engineering; Woodhead Publishing, 2019; pp 51–78. <https://doi.org/10.1016/B978-0-08-102293-1.00003-6>.
- (33) Mae, H.; Omiya, M.; Kishimoto, K. Effects of Strain Rate and Density on Tensile Behavior of Polypropylene Syntactic Foam with Polymer Microballoons. *Mater. Sci. Eng. A* **2008**, *477* (1), 168–178. <https://doi.org/10.1016/j.msea.2007.05.028>.
- (34) Mouhmid, B.; Imad, A.; Benseddiq, N.; Benmedakhène, S.; Maazouz, A. A Study of the Mechanical Behaviour of a Glass Fibre Reinforced Polyamide 6,6: Experimental Investigation. *Polym. Test.* **2006**, *25* (4), 544–552. <https://doi.org/10.1016/j.polymertesting.2006.03.008>.
- (35) Liu, H.; Li, Y.; Dai, K.; Zheng, G.; Liu, C.; Shen, C.; Yan, X.; Guo, J.; Guo, Z. Electrically Conductive Thermoplastic Elastomer Nanocomposites at Ultralow Graphene Loading Levels

- for Strain Sensor Applications. *J. Mater. Chem. C* **2015**, *4* (1), 157–166. <https://doi.org/10.1039/C5TC02751A>.
- (36) Beutier, C.; David, L.; Sudre, G.; Cassagnau, P.; Heuillet, P.; Cantaloube, B.; Serghei, A. In-Situ Coupled Mechanical/Electrical Investigations of EPDM/CB Composite Materials: The Electrical Signature of the Mechanical Mullins Effect. *Compos. Sci. Technol.* **2021**, 109144. <https://doi.org/10.1016/j.compscitech.2021.109144>.
- (37) Li, G.; Dai, K.; Ren, M.; Wang, Y.; Zheng, G.; Liu, C.; Shen, C. Aligned Flexible Conductive Fibrous Networks for Highly Sensitive, Ultrastretchable and Wearable Strain Sensors. *J. Mater. Chem. C* **2018**, *6* (24), 6575–6583. <https://doi.org/10.1039/C8TC01924J>.
- (38) Christ, J. F.; Aliheidari, N.; Pötschke, P.; Ameli, A. Bidirectional and Stretchable Piezoresistive Sensors Enabled by Multimaterial 3D Printing of Carbon Nanotube/Thermoplastic Polyurethane Nanocomposites. *Polymers* **2019**, *11* (1), 11. <https://doi.org/10.3390/polym11010011>.
- (39) Mullins, L. Effect of Stretching on the Properties of Rubber. *Rubber Chem. Technol.* **1948**, *21* (2), 281–300. <https://doi.org/10.5254/1.3546914>.
- (40) Mullins, L.; Tobin, N. R. Theoretical Model for the Elastic Behavior of Filler-Reinforced Vulcanized Rubbers. *Rubber Chem. Technol.* **1957**, *30* (2), 555–571. <https://doi.org/10.5254/1.3542705>.
- (41) Mullins, L.; Tobin, N. R. Stress Softening in Rubber Vulcanizates. Part I. Use of a Strain Amplification Factor to Describe the Elastic Behavior of Filler-Reinforced Vulcanized Rubber. *J. Appl. Polym. Sci.* **1965**, *9* (9), 2993–3009. <https://doi.org/10.1002/app.1965.070090906>.
- (42) Diani, J.; Fayolle, B.; Gilormini, P. A Review on the Mullins Effect. *Eur. Polym. J.* **2009**, *45* (3), 601–612. <https://doi.org/10.1016/j.eurpolymj.2008.11.017>.
- (43) Yeh, F.; Hsiao, B. S.; Sauer, B. B.; Michel, S.; Siesler, H. W. In-Situ Studies of Structure Development during Deformation of a Segmented Poly(Urethane–urea) Elastomer. *Macromolecules* **2003**, *36* (6), 1940–1954. <https://doi.org/10.1021/ma0214456>.
- (44) Liao, T.; Jiang, Z.; Li, R.; Gao, Y.; Men, Y. Stretching Temperature Dependence of the Critical Strain in the Tensile Deformation of Polyethylene Copolymer. *Eur. Polym. J.* **2017**, *97*, 188–197. <https://doi.org/10.1016/j.eurpolymj.2017.10.015>.
- (45) Koga, T.; Hashimoto, T.; Takenaka, M.; Aizawa, K.; Amino, N.; Nakamura, M.; Yamaguchi, D.; Koizumi, S. New Insight into Hierarchical Structures of Carbon Black Dispersed in Polymer Matrices: A Combined Small-Angle Scattering Study. *Macromolecules* **2008**, *41* (2), 453–464. <https://doi.org/10.1021/ma071867l>.
- (46) Ehrburger-Dolle, F.; Bley, F.; Geissler, E.; Livet, F.; Morfin, I.; Rochas, C. Filler Networks in Elastomers. *Macromol. Symp.* **2003**, *200* (1), 157–168. <https://doi.org/10.1002/masy.200351016>.
- (47) Rieker, T. P.; Hindermann-Bischoff, M.; Ehrburger-Dolle, F. Small-Angle X-Ray Scattering Study of the Morphology of Carbon Black Mass Fractal Aggregates in Polymeric Composites. *Langmuir* **2000**, *16* (13), 5588–5592. <https://doi.org/10.1021/la991636a>.
- (48) Chen, Q.; Xiang, D.; Wang, L.; Tang, Y.; Harkin-Jones, E.; Zhao, C.; Li, Y. Facile Fabrication and Performance of Robust Polymer/Carbon Nanotube Coated Spandex Fibers for Strain Sensing. *Compos. Part Appl. Sci. Manuf.* **2018**, *112*, 186–196. <https://doi.org/10.1016/j.compositesa.2018.06.009>.

- (49) Chen, D.; Yang, J.; Chen, G. The Physical Properties of Polyurethane/Graphite Nanosheets/Carbon Black Foaming Conducting Nanocomposites. *Compos. Part Appl. Sci. Manuf.* **2010**, *41* (11), 1636–1638. <https://doi.org/10.1016/j.compositesa.2010.07.013>.